CHALMERS
UNIVERSITY OF TECHNOLOGY

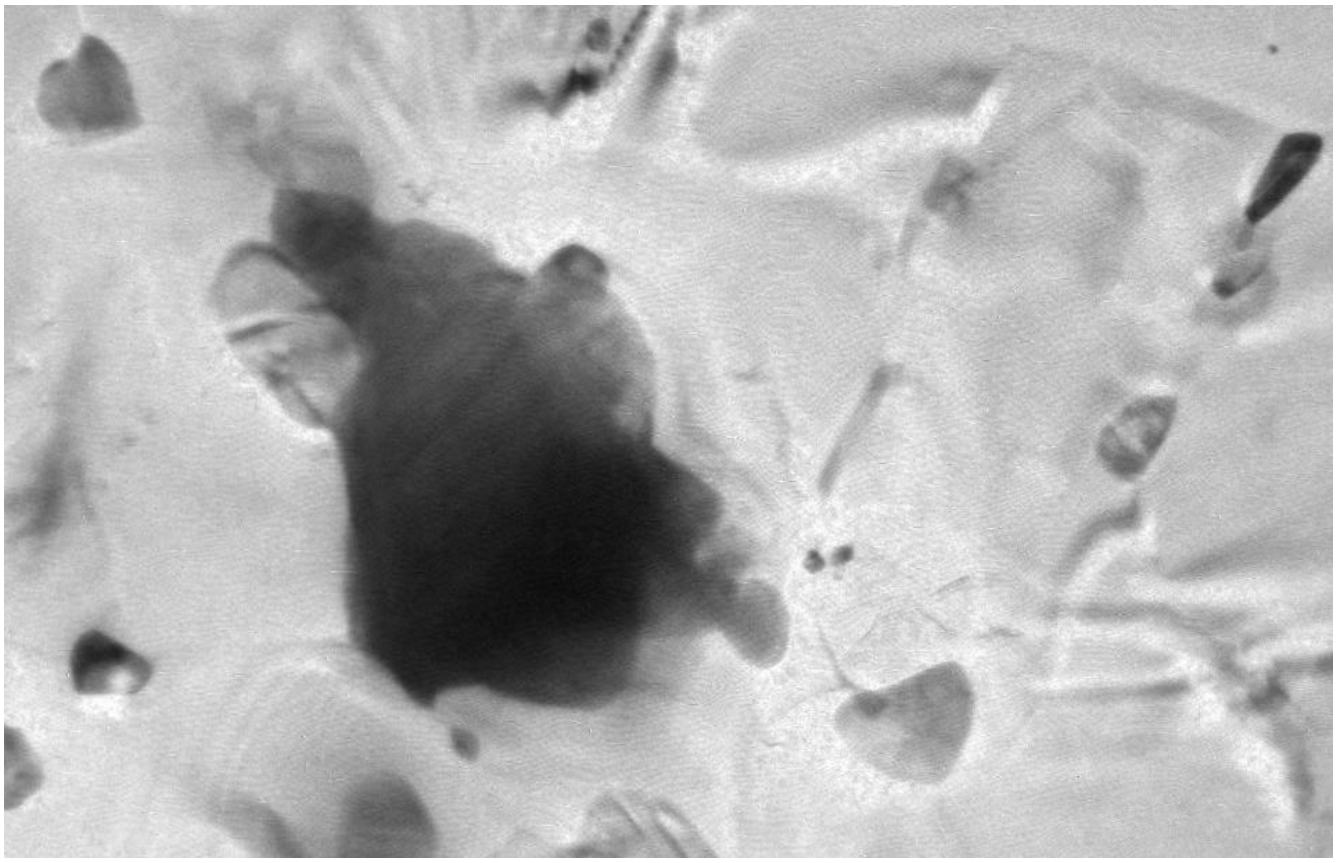

Microstructure evolution and creep resistance of a Z-phase strengthened 12% Cr steel

Master's Thesis in the Master's Programme Materials Engineering

JOHANNA TIMHAGEN

Department of Industrial and Materials Science
CHALMERS UNIVERSITY OF TECHNOLOGY
Gothenburg, Sweden 2019
Master's Thesis 2019

MASTER'S THESIS 2019

Microstructure evolution and creep resistance of a Z-phase strengthened 12% Cr steel

Master's Thesis in the Master's Programme Materials Engineering

Johanna Timhagen

Department of Industrial and Materials Science
Division of Materials and Manufacture
CHALMERS UNIVERSITY OF TECHNOLOGY
Gothenburg, Sweden 2019

Microstructure evolution and creep resistance of a Z-phase strengthened 12% Cr steel

Master's Thesis in the Master's Programme Materials Engineering

JOHANNA TIMHAGEN

Examensarbete 2019/ Institutionen för industri- och materialvetenskap,
Chalmers tekniska högskola 2019

Department of Industrial and Materials Science
Division of Materials and Manufacture
Chalmers University of Technology
SE-412 96 Gothenburg
Sweden
Telephone: + 46 31 772 1000

Cover:
TEM micrograph showing various particles in sample ZL3 LY aged for 30 307 h.
Department of Industrial and Materials Science, Gothenburg, Sweden, 2019

Microstructure evolution and creep resistance of a Z-phase strengthened 12% Cr steel

Master's thesis in the Master's Programme Materials Engineering

JOHANNA TIMHAGEN
Department of Industrial and Materials Science
Chalmers University of Technology

ABSTRACT

9–12% Cr steels are a family of steels, which are the backbones for today's fossil fuel steam power plants, which provide more than 60% of electricity worldwide. By developing more creep and corrosion resistant 9–12% Cr steels, the operation temperature of 620°C could be increased to 650°C, which would reduce the environmental impact. For improved resistance to corrosion, a higher Cr content is needed. However, an increased Cr content results in formation of stable but big detrimental Z-phase precipitates. While Z-phase traditionally results in premature creep failures, a new alloy design strategy, called Z-phase strengthening, aims to make use of Z-phase particles as strengthening precipitates rather than detrimental particles.

Getting a better understanding of the correlation between microstructure evolution and creep resistance in these steels, could potentially lead to a solution to the conflict between creep and corrosion resistance at 650°C. In this study, two versions of the same 12% Cr steel have been evaluated, one version is tempered at 700°C and the other at 740°C. Investigation have been done with light optical microscopy (LOM), scanning electron microscopy (SEM), transmission electron microscopy (TEM) and energy dispersive X-ray spectroscopy (EDX). Results from these methods were correlated with results from mechanical testing and creep testing, and together they provided a better understanding of the evolution of nano-sized particles at high temperatures.

It was found that tempering with a lower temperature results in better creep properties. Mechanical properties are also improved by a lower tempering temperature, but eventually the values of hardness, tensile testing, and impact toughness for the two different versions coverage with ageing. $M_{23}C_6$ particles grow very slowly. Laves-phase is significantly affected by tempering temperature. A higher tempering temperature results in Z-phase particles that start to transform from MX particles after a shorter ageing time. The average particle size is smaller with a lower tempering temperature. A lower tempering temperature results in superior microstructure regarding nano-sized particles.

Key words: creep, precipitation hardening, scanning electron microscopy, transmission electron microscopy, CrTaN, MX, $M_{23}C_6$, Laves-phase, BN, tempering temperature, heat treatment.

Mikrostrukturutveckling och krypmotstånd i ett Z-fasförstärkt 12% Cr stål
Examensarbete inom mastersprogrammet Materials Engineering

JOHANNA TIMHAGEN
Institutionen för industri- och materialvetenskap
Chalmers tekniska högskola

SAMMANFATTNING

9–12% Cr stål är en familj av stål, som är grundpelare för dagens ångkraftverk för fossila bränslen, vilka genererar över 60% av elproduktionen världen över. Genom att utveckla mer kryp- och korrosionsresistenta 9–12% Cr stål, skulle driftstemperaturen kunna ökas från 620°C till 650°C, vilket skulle minska miljöpåverkan. För bättre korrosionsresistens krävs högre andel Cr. En högre andel Cr resulterar emellertid i bildning av ett stort antal stabila men stora Z-faspartiklar. Medan Z-fas traditionellt resulterar i prematura brott, strävar en ny legeringsdesignstrategi, kallad Z-fasförstärkning, att använda Z-faspartiklar som förstärkande partiklar, istället för skadliga partiklar.

En förbättrad förståelse av sambandet mellan evolutionen av mikrostruktur och krypmotstånd i dessa stål kan potentiellt leda till en lösning av konflikten mellan kryp- och korrosionsresistens, vid 650° C. I denna studie har två varianter av samma 12% Cr-stål utvärderats, där den ena varianten anlöpts vid 700°C och den andra vid 740°C. Varianterna har undersökts med ljusmikroskopi (LOM), svepelektronmikroskopi (SEM), transmissionselektronmikroskopi (TEM) och energidispersive töntgenspektroskopi (EDX). Resultaten från dessa metoder inkorporerades med mekanisk provning och krypprovning, och tillsammans har de gett en bättre förståelse för utvecklingen av partiklar i nanostorlek vid höga temperaturer.

Det har visat sig att anlöpning vid en lägre temperatur resulterar i bättre krypegenskaper. Mekaniska egenskaper förbättras också med lägre anlöpningstemperatur, dock konvergerar värden för de två olika varianterna i slutändan. $M_{23}C_6$-partiklar växer mycket långsamt. Lavesfas påverkas signifikant av anlöpningstemperatur. En högre anlöpningstemperatur resulterar i att Z-faspartiklar omvandlas från MX-partiklar efter en kortare åldringstid. Den genomsnittliga partikelstorleken är mindre med en lägre anlöpningstemperatur. En lägre anlöpningstemperatur resulterar i en överlägsen mikrostruktur, avseende partiklar i nanostorlek.

Nyckelord: kryp, utskiljningshärdning, CrTaN, MX, $M_{23}C_6$, Lavesfas, BN, svepelektronmikroskopi (SEM), transmissionselektronmikroskopi (TEM), anlöpningstemperatur, värmebehandling.

Acknowledgements

First of all, I would like to express my greatest gratitude to my supervisor and examiner at Chalmers, Associate Professor Fang Liu, who made me excited about this project from the very beginning and have with patience and enthusiasm guided me through it.

I would like to sincerely thank Siemens Industrial Turbomachinery AB in Finspång, for giving me the opportunity to be part of this project and for providing financial support. Especially a warm thank you to my supervisor at Siemens, Lennart Johansson, who provided great insight to creep and mechanical testing, and have kindly introduced Siemens and Finspång to me.

Thank you to Senior Professor Hans-Olof Andrén, at the Department of Physics, who not only gave me a better insight to the world of research, but who realized early on that investigation in SEM would not be enough to analyses the desired particles and steered this project to include a larger part of analyses in TEM.

A special thank you to Irina Fedorova, PostDoc at the Department of Physics, who have been of great help in the preparation of extractive carbon replicas.

Thank you to the professors and personal at the Department of Industrial and Materials science, in particular, Yiming Yao, who introduced me to the SEM at the department, and taught me metallographic sample preparation of self-supporting TEM samples.

Thank you to my follow master thesis colleague at the department, who have been a great moral support during lunches and fika. Thank you to my friends, who have been there, then I have needed to get away for a bit.

Finally, a loving thanks to my family, who does not really understand what I have actually been studying, but have always been supportive, no matter what I decide to take on next.

Gothenburg, June 2019

Johanna Timhagen

Contents

List of Abbreviations

APT	Atom Probe Tomography
bcc	Body Centred Cubic
bct	Body Centred Tetragonal
BSE	Backscattered Electron
EDX	Energy Dispersive X-ray Spectroscopy
fcc	Face Centred Cubic
FEG	Field Emission Gun
hcp	Hexagonal Close Packed
HY	High Yield
LOM	Light Optical Microscopy
LY	Low Yield
M_f	Martensitic finish temperature
M_s	Martensitic start temperature
PAGB	Prior Austenite Grain Boundary
SE	Secondary Electron
SEM	Scanning Electron Microscopy
STEM	Scanning Transmission Electron Microscopy
TEM	Transmission Electron Microscopy

List of Figures

1 Introduction

In this chapter the background and the aim of the project is presented first, followed by the research questions and limitations.

1.1 Background

This work is performed in collaboration with Siemens , a global leader in producing energy-related equipment, e.g. steam turbines for steam power plants. 9–12% Cr steels are a family of steels, which are the backbones for today's fossil fuel steam power plants, which provide more than 60% of electricity worldwide.

Today's best 9–12% Cr steels are limited to an operation temperature of 620°C. While austenitic steels can be used at 650–700°C and Ni base super alloys can be used at even higher temperature, 9–12% Cr martensitic steels have better properties regarding the thermal conductivity and the thermal expansion coefficient. 9–12% Cr steels also contain less expensive alloying elements, and thus less expensive. By developing and deploying more creep and corrosion resistant 9–12% Cr steels at 650°C, the operation temperature of these plants could be increased, and the environmental impact would be reduced [1].

For an increased operation temperature, improved resistance to corrosion and increased creep strength is necessary. Applying expensive coating to the already existing 9% Cr steels to protect them from oxidation is not desirable, which means alloying with higher Cr content is needed for improving the corrosion resistance. An increased Cr content results in formation of a large number of stable but big Z-phase precipitates, which traditionally decrease the creep strength and result in premature failures. The conflict between creep and corrosion resistance in 9–12% Cr steels, is tackled by a new alloy design strategy called Z-phase strengthening, which aims to make use of Z-phase particles as strengthening precipitates rather than detrimental particles [2].

1.2 Aim

The aim of this project is to gain a deeper understanding of the correlation between microstructure evolution and creep resistance in a new generation of Z-phase strengthened 12% Cr steels. The knowledge gained within this project on the behaviour of nanosized particles at high temperatures can lead to a potential solution to the conflict between creep and corrosion resistance at 650°C for these steels.

1.3 Research questions

To find a potential solution to the conflict between creep and corrosion resistance at 650°C for 12% Cr steel, the following questions should be evaluated:

- What is the difference in microstructure between the as-tempered 12% Cr steel and the long-term thermally aged samples?
- What are the effects of the chemical composition and heat treatment on nano-sized particles?
- How do nano-sized particles evolve at high temperatures?

1.4 Limitations

In previous studies, the effect of different alloying elements on Z-phase have been evaluated. For example, the effect of Cu and C on the mechanical properties of 9–12% Cr steels were studied. The coarsening behaviour of trial steels containing Z-phase with both Ta and Nb was compared with pure Ta-based Z-phase. The next stage is to evaluate the effect of tempering temperature on mechanical properties and creep behaviour. Therefore, the study is limited to:

- One type of trial steel, that is a pure Ta-based Z-phase strengthened 12% Cr steel, called ZL3.
- Comparison of two different versions of steel ZL3, which have different tempering temperatures, 700°C and 740°C.
- Evaluation of samples thermally aged for 3 000 h, 10 000 h and 30 307 h at 650°C, compared with the as-tempered steel.

1.5 Thesis outline

There are five chapters followed. Chapter 2 presents a theoretical background, to provide a better understanding of the research topic. Specifically, Chapter 2 handles the basics of iron and steel, the characteristics of creep and thermal ageing, and some important aspects on 9–12% Cr steels, such as heat treatment, strengthening mechanisms and different families of precipitates, and a special emphasis is put on Z-phase formation.

Chapter 3 deals with the methodology used for this study. The material and the heat treatment are described, followed by the mechanical testing methods. Furthermore, the techniques of light optical microscopy (LOM), scanning electron microscopy (SEM) and transmission electron microscopy (TEM), and the sample preparation for these techniques are described.

Chapter 4 analyses the results obtained from the investigation of the test material ZL3. Mechanical testing is presented first, in the form of diagrams, showing creep properties, the hardness, the yield strength, the ultimate tensile strength and the impact toughness. After this, evaluation of prior austenite grain size, and evaluation of primary and secondary particles are presented. Chapter 5 discusses the correlation between the microstructure and the mechanical properties. In the final part, Chapter 6, the conclusions are summarised.

2 Theory

For better understanding of the results presented in later chapters, a theoretical background is provided in this chapter. The chapter goes through the basics of iron and steel, and thermal degradation of metals, such as creep and thermal ageing. Furthermore, some important aspects on 9–12% Cr steels are introduced, including heat treatment, strengthening mechanisms and different families of precipitates, especially focusing on Z-phase formation.

2.1 Iron and Steel

In pure bulk iron there are three allotropes that can occur. These are body-centred cubic (bcc), also known as α-iron or ferrite, face-centred cubic (fcc), also known as γ-iron or austenite, and hexagonal close-packed (hcp), also known as ε-iron. The phase diagram for Fe-C is shown in *Figure 2.1*. The bcc structure is stable from room temperature up to the A_3 point at 910°C. From 910°C the fcc structure is stable until 1390°C (the A_4 point), at this point the bcc structure become stable again and is now called δ-ferrite. Finally, at 1536°C pure iron reaches its melting point. Meanwhile, ε-iron only occurs at extremely high pressure [3].

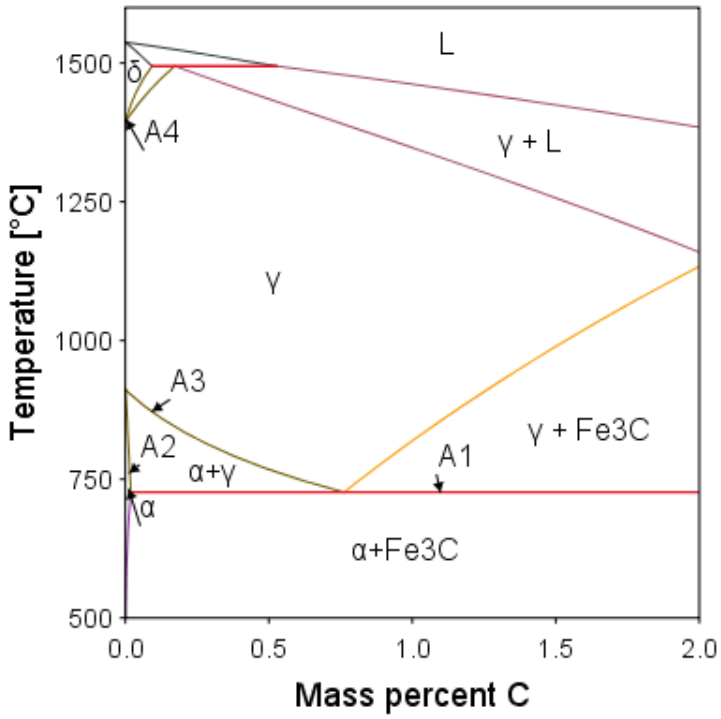

Figure 2.1 Phase diagram of Fe-C, showing up to 2 wt.% C.

The most successful iron alloy, and also one of the most dominant materials used today overall, is steel. For an iron alloy to be classified as steel, it is generally considered to consist of up to 2 wt.% C. Moreover, steels are divided into three subgroups. Steels with up to 0.3 wt.% C are called low carbon steels. Steels with a carbon content between 0.3 and 0.8 wt.% are classified as medium carbon steels. Steels with a carbon content higher than 0.8 wt.% are classified as high carbon steels. The microstructure of steel differs from that of pure iron. Most notably, from room temperature up to 738°C (the A_1 point), the microstructure consists of alternating plates of ferrite and cementite

(Fe_3C). This phase is also called pearlite. The varying microstructures and properties that steels provide, combined with its cost-efficiency, are reasons behind why more than a billion tonnes are consumed annually [1,3].

2.2 Thermal degradation of metals

Elevated temperatures affect the microstructure of steels. Understanding the influence of temperature on microstructure gives an important insight into the resulting properties. Therefore, the process of thermal ageing is presented. Moreover, temperature combined with mechanical stress, causes additional challenges in the form of creep, which is also introduces in the following sub-section.

2.2.1 Thermal aging

Thermal aging is used to test how the properties and microstructure changes under the pure influence of high temperature. Testing, such as tensile, hardness, and impact testing, is done for different ageing times [4].

2.2.2 Creep

Creep is a state, where a material experiences a fixed mechanical stress for a period of time, when the plastic deformation is slow and continuous. While creep can occur at any temperature above zero Kelvin, it is more commonly associated with elevated temperatures [1,5]. When testing a material's creep strength, it is usually done at a constant temperature and load. The result is often presented in creep curves [1], which can be seen in *Figure 2.2*. There are normally three stages of creep:

1. Primary creep: The creep rate decreases when the strain increases, due to strain hardening.
2. Secondary/Steady-state creep: The creep rate remains constant with increasing strain, due to steady generation and recovery of dislocations.
3. Tertiary creep: The creep rate increases with the formation of necking and cavities, which continues until rupture [6].

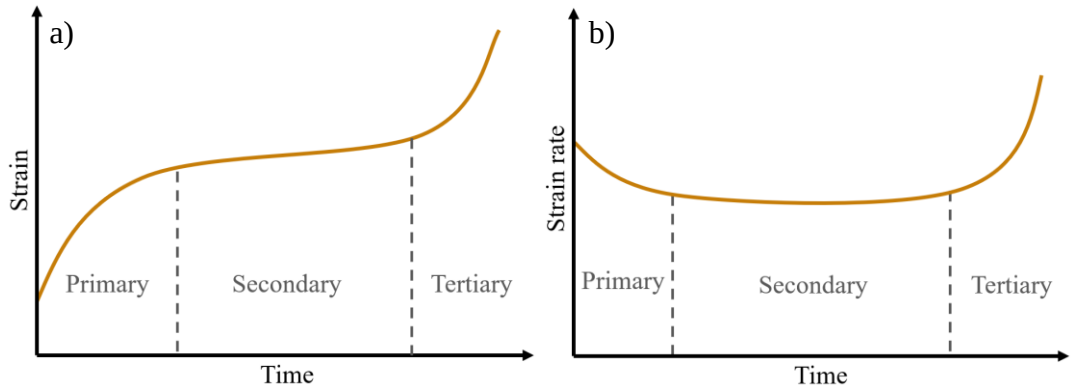

Figure 2.2 Schematic drawing of a) a creep curve and b) a creep rate curve.

The stages of creep behave slightly different for creep-resistant 9-12% Cr steels. Instead of continuing to secondary creep after primary creep, tertiary creep begins directly [1]. The creep mechanism in 9–12% Cr steels is typically either dislocation climb or

dislocation glide controlled. Dislocations move easier in pure metals, as there are very few obstacles within the perfect fcc, bcc or hcp lattice planes. However, it is harder for dislocations to move out of the planes, which means that the dislocations have to be eliminated either through gliding or climbing. Climbing (edge dislocations) is the motion of jogs and is dependent on the formation and migration of vacancies. Gliding is instead the motion of screw dislocations, which in contrast are dependent on the diffusion of solute atoms instead of vacancies. The solute atoms diffuse and gather together, which leads to the formation of precipitates. In the early stages of creep these precipitates are small but many, which is an advantages for creep resistance, but with time the particles grow larger and become fewer [7].

2.3 9–12% Cr steels

Martensitic 9–12% Cr steels are one of the most important high temperature materials used today. Their high performance for critical properties, such as creep strength, oxidation and corrosion resistance, thermal conductivity and thermal expansion, is what makes them attractive. Furthermore, they are produced at a relatively low cost, especially compared to the more expensive creep resistant austenitic stainless steels and nickel-base superalloys. Applications for 9–12% Cr steels can be found in power plants, both conventional and nuclear plants, as thick-section components, e.g. main steam pipes, steam turbine rotors, and turbine housing [1,8].

The 9-12% Cr steels typically have a carbon content below 0.1 wt.%. Other common alloying elements are: Ni, Mn, Co, Si, Mo, Cu, W, Nb, V, N, and B. Alloying elements are traditionally divided into either austenite stabilizers or ferrite stabilizers. Austenite stabilizers can increase the A_4 temperature and lower the A_3 temperature. In steels, addition of C, N, Mn, Ni, Cu, and Co has this effect. The opposite is true for ferrite stabilizers. These alloying elements instead decrease the A_4 temperature and increase the A_3 temperature. Common ferrite stabilizers are Si, Mo, W, V, Nb, and Ti [1]. The alloying elements also affect the M_s temperature. For 9–12% Cr steels, the M_s temperature is around 400°C and the M_f temperature is around 200°C.

The martensitic structure contains prior austenite grain boundaries (PAGB). Within the PAGB, packets are formed, which in turn consist of 10-20 plates of laths. Moreover, coarse precipitates tend to nucleate and grow along the PAGB [1, 9,10].

2.3.1 Heat treatment

The sequence of heat treatments for 9–12% Cr steels generally starts with austenitization and quenching, followed by one step or several steps of tempering treatments. *Figure 2.3* shows how these procedures relate to each other time and temperature wise.

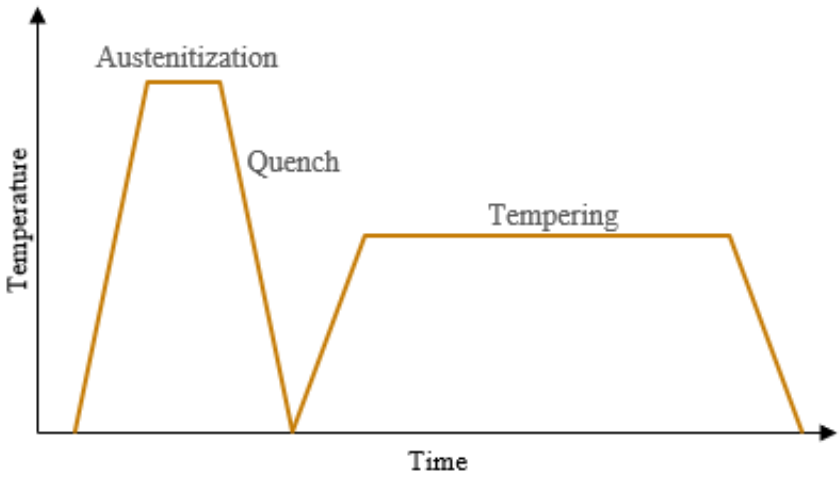

Figure 2.3 Schematic illustration of common heat treatment of 9-12% Cr steels.

Austenitization

During austenitization the steel is heated above the A_3 point and into the austenite field, see *Figure 2.1*. At this point the austenite grains start to nucleate and grow. The steel is held there for enough time so nitrides and carbides start to dissolve. The selection of austenitization temperature is a fine balance. At a high temperature more nitrides and carbides dissolve into the steel and form solid solution, and consequently more secondary precipitates in the later stages. On the other hand, undissolved primary particles pin the grain boundaries and restrict the grain growth. The typical austenitization temperature is between 1020°C and 1150°C [1,11].

Quenching

If a steel is slowly cooled from the austenite field, the resulting microstructure consist of alternating plates of ferrite and cementite, also called pearlite [11]. With quenching, which means that the alloy is rapidly cooled from the austenite field, the aim is instead to obtain a body centred tetragonal (bct) structure. In the fcc structure there is more place for interstitial solute atoms, like carbon and nitrogen, to fit between the lattice, compared with the bcc structure. As a result, carbon and nitrogen atoms are rejected from the fcc structure during slow cooling. In contrast, the bct structure, also called martensite or α'-iron, is a super-saturated solid solution of carbon or nitrogen. During cooling the interstitial atoms do not have enough time to diffuse out of the fcc structure, and instead get trapped within the martensite. Martensite is a thermodynamically unstable phase [1,11,12].

When quenching, the formation of phases like ferrite and pearlite needs to be avoided. Therefore, it is important to have a sufficiently high cooling rate. The transformation of martensite does not occur until the martensite starting temperature, M_s, is reached [11,12]. However, it is not always attainable to get a fully martensitic structure. Some untransformed austenite, referred to as retained austenite, may still be found after the quenching process. As a result, the point, where 95% of the martensitic transformation is complete, is often defined as the martensite finish temperature, M_f [12]. To achieve high enough cooling rates, different types of cooling medium can be used. The most common ones are water and oil, but other methods like air blasting is also often used [11].

Tempering

During tempering the material is kept at an intermediate temperature, below the A_1 point, to reduce the residual stresses left in the material after quenching. While this process decreases the strength and hardness that was introduced during quenching, the material also gains back some of the ductility and toughness that was lost. The tempering temperature have a significant impact on the mechanical properties. The hardness was shown to decrease with increasing tempering temperature. Sometimes more than one tempering treatments are conducted in stages, starting with a lower temperature and then increasing the temperature step by step [1,11].

Equally important during tempering is the formation of secondary precipitates. The small precipitates start to from when carbon and nitrogen are rejected from the strained bct structure, and thus resulting in formation of carbides and nitrides [12].

2.3.2 Strengthening Mechanisms

The strength, ductility and toughness of alloys depend on their microstructure. The microstructure can be manipulated and tailored to obtain desirable combination of properties for diverse applications [13]. The four strengthening mechanisms are solid solution hardening, precipitation hardening, dislocation hardening and sub-boundary hardening. Even if a combination of mechanisms are used, for creep resistant steels precipitation hardening is considered the most important strengthening mechanism [1,14].

Solid solution hardening

Solid solution hardening is when alloying elements are carefully added as solute into the alloy to strengthen the material. The alloying atoms are often smaller or larger than the host atoms. As a result, strain energy arises in the matrix, which acts as a barrier for dislocation climb and glide, thus increasing the materials strength. The alloying atoms either act as substitutional or interstitial atoms. Substitutional atoms, are when larger or in some cases smaller atoms, change place with the host atoms. In contrast, interstitial atoms are when smaller atoms do not take the host atoms place, but instead fit in between them [13]. Efficient solid solution strengthening atoms in 9–12% Cr steels, are substitutional atoms of Mo and W. However, during service these alloying elements form precipitation of $Fe_2(W, Mo)$, called Laves-phase, and decrease the solid solution strengthening effect [1].

Precipitation hardening

In supersaturated conditions, solute atoms are trapped in the matrix. With enough time and temperature, precipitation occurs - the solute atoms will form new chemical compounds, precipitates. When the precipitates are small they fit more or less coherently within the matrix, which strengthen the material through strain energy. Precipitates at this size also become pinning sites for dislocations, which is in direct correlation to the creep strength. When the precipitates grow, they become more and more incoherent with the matrix. Consequently, the material exhibit an increase in ductility and a reduction in hardness and strength [13].

In 9–12% Cr steels, precipitates tend to be distributed at the grain and lath boundaries as well as within the matrix. Precipitates which have a positive effect on the strength are: $M_{23}C_6$, MX, and Laves-phase. With increasing temperature, the dislocations climb more easily and the effect of precipitation hardening decreases. This makes the material more sensitive to creep at higher temperatures [1].

Dislocation hardening

When the lattice is free from disruptions, dislocations can easily travel through the lattice. By introducing a higher number of dislocations, and by creating more disruptions in the lattice, the dislocations get entangled with each other and their movement is decreased. Hence, the strength is increased, and the ductility is decreased. Both cold working and formation of martensite can introduce a high number density of dislocations in the material [1,13].

Sub-boundary hardening

Grain boundaries have higher energy than the grains, which results in the boundaries acting as barriers for dislocations. Therefore, rather than continuing forward, the dislocation movements will be pinned by the boundaries. This leads to an increase in not only strength, but also ductility and toughness. With smaller grains there will be a higher fraction of grain boundaries, which improves the above mentioned properties [13]. With the primary precipitates, the grain boundaries are stabilized during austenitization, which is important for the creep resistance in 9–12% Cr steels [1].

2.3.3 Precipitates in 9–12% Cr steels

In 9–12% Cr steels the typically precipitates are: carbides such as $M_{23}C_6$, carbonitrides as MX, nitrides as M_2X and Z-phase, and intermetallic as Laves-phase. Precipitates that remain from the austenitization treatment are called primary particles. Particles that instead form during the tempering treatment or later on during service, are called secondary particles. Majority of precipitation processes follow the classic precipitation theory, which begins with nucleation, and continues with growth and coarsening.

Precipitation process

The nucleation rate of precipitation depends on the thermodynamic driving force, the interfacial energy, as well as the accessibility to necessary elements form the matrix [1,15]. The thermodynamic driving force is greater at the following places in decreasing order: free surfaces, grain boundaries and interphase boundaries, stacking faults, dislocations, vacancies, and homogeneous sites [16]. With a low nucleation rate, the particles grow bigger, which dilutes the matrix and decreases the chance for new precipitates to nucleate. This has a negative effect on the precipitate hardening effect and thus the creep strength. Therefore, a high nucleation rate is preferable, since it enables a larger number of finely distributed particles [1,15].

When the clusters reach a certain critical size the growth phase takes off. The growth phase, like the nucleation phase, is controlled by the thermodynamic driving force, the interfacial energy, and the accessibility to necessary elements in the matrix, therefore

the diffusion rate. The precipitates grow both in size and volume fraction during the growth phase and continue to do so until the system is thermodynamically stable [1,15].

The last stage of precipitation is coarsening. During this phase no new precipitates nucleate [15]. Instead, diffusion of solute from small particles to larger particles will occur [16]. Of the same volume, small particles have higher surface area compared to larger particles. Therefore, it is energetically beneficial for precipitates to coarsen, since the total interfacial energy will decrease [1,15]. The consequence of this is a loss of precipitation hardening, and thus a decrease in mechanical properties, most notably the creep strength [16].

Metastable precipitates

Not all particle compositions are thermodynamically stable to survive longer times and will instead dissolve or transform to other precipitates during exposure to high temperatures. These particles are overtaken by more stable ones, such as MX by Z-phase. Whether the particles are stable or not, is decided by the thermodynamic driving force. Typical metastable phases in 9–12% Cr steels are M_3C, M_7C_3, and MX [1,15].

$M_{23}C_6$

$M_{23}C_6$ have a cubic crystal structure. For 9–12% Cr steel the M generally stands for Cr. Smaller amount of Fe, Mo, W, and B can also be dissolved. During the heat treatment, $M_{23}C_6$ replace metastable phases such as M_3C and M_7C_3 [1]. $M_{23}C_6$ particles precipitate predominantly at the prior austenite grain boundaries and the martensite lath or subgrain boundaries, which is attributed to the lower energy there compared to the inside of the matrix [17,18,19]. This family of precipitates are often located at the boundaries, pin the boundaries, and contribute to sub-boundary and precipitation hardening [1]. After tempering the size of the $M_{23}C_6$ carbides was reported approximately 78 nm; and after 8 000 hours of creep testing the size increased to 103 nm [17]. Boron in 9–12% Cr steels often enrich the $M_{23}C_6$ carbides, which slows down the coarsening rate of $M_{23}C_6$, and thus increases the creep strength [20].

Laves-phase

The Laves-phase often have the chemical composition $Fe_2(W,Mo)$, and form a hexagonal crystal structure. Laves-phase mainly contain W and/or Mo, as well as traces of Cr and Si [1,21]. The shape of the Laves-phase particles is often not spherical but irregular and tend to form clusters along the martensite lath boundaries or sub-grain boundaries. They also have a preference to form close to $M_{23}C_6$ carbides [17,21]. Laves-phase are secondary particles that form relatively quickly during thermal service [22].

The potential benefit or drawback of the Laves-phase formation have been debated [21]. W and Mo provide solid solution strengthening within the matrix, but formation of Laves-phase cause depletion of W and consequently decrease the solid solution strengthening effect [1,21]. However, due to the preferential distribution of the Laves-phase along boundaries, it provides excellent precipitation hardening and creep resistant at the beginning of their formation [21]. With coarsening the hardening effect decreases. Additionally, the material has the risk of becoming brittle. Therefore, controlling the coarsening is vital. Laves-phase containing W nucleate faster and lead

to a finer distribution of Laves-phase. W-containing Laves-phase is thus preferred to Mo-containing Laves-phase [1].

BN

Formation of BN particles occur during slow cooling after solidification, which consume beneficial alloying elements of B and N. This has a negative impact on the mechanical properties [23,24]. Especially the consumption of N affects formation of secondary particles, and consumption of B affects the coarsening behaviour of secondary particles, such as $M_{23}C_6$ and Z-phase precipitates. With less B in the matrix, the secondary particles grow coarser, which decrease the effect of precipitation hardening [24]. The formation of BN particles is easier with a higher C content, since it increases the activity of B. On the other hand, activity of N is decreased by a higher Cr content, which makes formation of BN more difficult [23].

MX

In 9–12% Cr steel, MX carbonitrides acts as one of the most effective precipitates for strengthening [22]. M stands for V, Nb, or Ta, while X stands for C and/or N. The MX carbonitrides are either coherent or semicoherent, and they precipitates at prior austenite grain lath and block boundaries, as well as within the matrix [1,17]. In 9–12% Cr steels there are different types of MX particles and they generally have slow coarsening rates. MX precipitates of the type NbC are typically spherical and remain from the austenitization treatment, which makes them primary particles. The MX particles of the type V(C,N) are instead formed during the tempering treatment, and are thus secondary precipitates and are more finely dispersed [1]. Ta-based MX particles are either primary or secondary particles and exists in several different forms, from almost pure TaN to Ta(C,N) with very high C content [23].

M_2X

M_2X particles have a hexagonal crystal structure. In 9–12% Cr steel the M_2X particles are often of the type Cr_2N, but Cr can also be replaced partly by V, Nb, and Ta [1]. It was reported that the formation of M_2X precipitates is influenced by the tempering temperature, especially in steels with a Cr content of 9 wt.%. [25,26]. With a tempering temperature below 720°C, large amounts of M_2X particles are more likely to form, than with a tempering temperature above 750°C. This was found be the case, regardless of the change in chemical composition of the M_2X particles during different tempering temperatures [25]. Consequently, lower tempering temperature promotes the formation of M_2X instead of MX [26]. At tempering temperature above 760°C, no M_2X particles was found [1]. However, the Cr content has also been found to have an influence of the stability of M_2X particles. For 12% Cr steels, formation of M_2X particles were shown, even after a tempering temperature above 780°C [26].

Z-phase

Z-phase have the chemical composition CrMN, there M stands for V, Nb or Ta. In the temperature range of interest, Z-phase is the most stable nitride, in 9–12% Cr steels [15]. Z-phase generally precipitates either through direct transformation from MX particles or by nucleation and growth from MX or M_2X particles, which is described more closely in sub-sections 2.4.1 and 2.4.2. Since Z-phase grow foremost from MX

particles, they are found at the same locations as MX particles. Namely, at prior austenite grain boundaries as well as lath and block boundaries, and within the sub-grains [27]. The morphology of Z-phase ranges from thin faceted plates in V-based Z-phase steels [28] to smaller and tetragonal shaped Nb-based Z-phase in austenitic steels [29].

2.4 Z-phase strengthened steels

9-12% Cr steels are often used in fossil fuel steam power plants. They are one of the most important high temperature materials. However, to increase the efficiency of the power plants, it is desirable to increase the service temperature further, preferably to a target temperature of 650°C. To achieve this, not only oxidation protection need to be improved, but also the creep strength need to be doubled [2]. Improved oxidation protection, without applying expensive coating, is accomplished by increasing the Cr content from 9% to 12%. The dilemma is that a higher Cr content is the driving force for forming stable Z-phase precipitates, which nucleate at the expense of beneficial MX particles, and result in premature failures [1,2].

An effort to avoid the formation of Z-phase was made. The idea was to avoid M_2X precipitates, since their composition is close to that of Z-phase and the energy barrier for their nucleation is very low [30]. Unfortunately, this did not succeed. Since Z-phase is thermodynamically stable and unavoidable given long enough time at elevated temperature, a new idea was coined by Danielson and Hald [2], called Z-phase strengthening. If Z-phase instead of MX was introduced with quick precipitation and fine distribution, the steel would benefit from the particles through precipitation hardening. This would mean that both the creep strength and the oxidation resistance would improve at the same time [2].

Z-phase does not appear in as-quenched steels; thus, they are secondary precipitates [28]. Experimental studies, as well as studies at various temperatures, have shown that Z-phase precipitate fastest at 650°C [2,28]. Two mechanisms for Z-phase transformation have been discovered, which is presented in the following sub-sections, 2.4.1 and 2.4.2.

2.4.1 MX to Z-phase transformation

Z-phase transformation from MX particles was found to have two different mechanisms. The first mechanism, see *Figure 2.4*, describes direct transformation from Cr-enriched MX particles to Z-phase [31]. Particles were found, that had a centre region of Cr-depleted (V,Nb)N particles with a rim, with a composition close to that of Z-phase. These regions have an even transition and the particles are referred to hybrid particles. That the (V,Nb)N regions starts out as Cr-enriched and transform into Cr-depleted, suggest that Z-phase transform by consuming Cr, V, Nb and N directly from the host particle. Thus the steel matrix is not the sole provider of Cr atoms to the Z-phase [28].

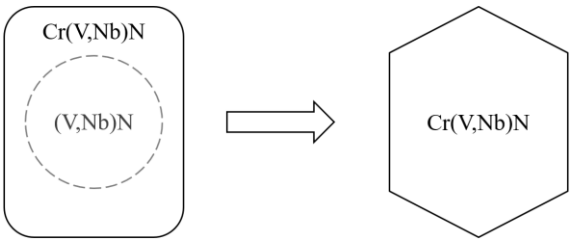

Figure 2.4 Z-phase transformation by direct transformation from MX particles [28].

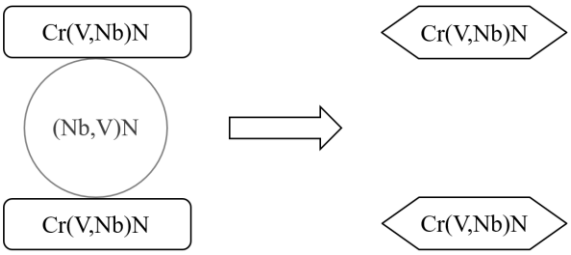

Figure 2.5 Z-phase transformation by nucleation and growth from MX particles [28].

The second mechanism seen in *Figure 2.5*, describes transformation from MX particles to Z-phase, by nucleation and growth from the MX particles. In this case the MX particles are Nb-rich (Nb,V)N particles. Z-phase start to form on each side of the (Nb,V)N particle by consuming Nb, V and N directly from the host particle. While at the same time consume Cr atoms from the surrounding matrix. Thus Z-phase transform at the expense of the MX particles [28].

2.4.2 M_2N to Z-phase transformation

It was suggested by Kim et al. [31] that Z-phase can grow not only from MX particles, but from M_2X as well. Analysis of a 11% Cr steel with high nitrogen content, showed that during aging, precipitation of Cr_2N and Nb(C,N) decreased, while precipitation of Z-phase increased. Similar result was achieved with creep testing, there Cr_2N almost disappeared and Z-phase once again increased [31].

Z-phase transformation from M_2X is believed to start with Cr_2N particles with a V-enriched rim. The V-rich rim arises due to the high solubility of V in Cr_2N. When V diffuses into Cr_2N and reach the same levels as Cr, the composition is close to that of Z-phase (CrVN). This then become a nucleation site for Z-phase, which can be seen in *Figure 2.6*. The Z-phase precipitates start to rapidly grow outwards and their size ends up exceeding that of the Cr_2N precipitates, whose size remain more or less the same. Thus, it is suggested that Z-phase transform through nucleation and growth from Cr_2N precipitates [31].

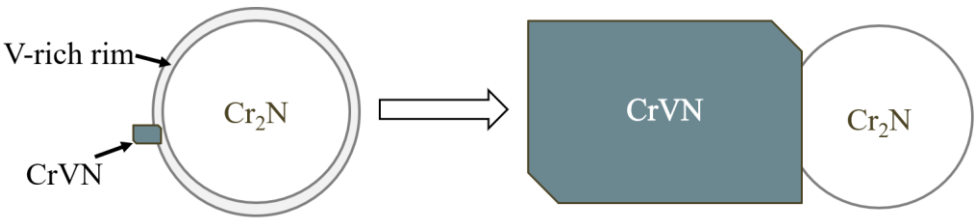

Figure 2.6 Z-phase transformation from M_2X particle [31].

2.4.3 Tantalum-based Z-phase

For Z-phase strengthened steels a fine distribution of Z-phase is necessary. This means that the formation of Z-phase must be quick. While the formation of V-based Z-phase is slow and Nb-based results in coarse precipitates, Ta-based Z-phase was found to form a fine distribution of precipitates [23,24]. If Ta is present together with Nb, the result is coarser Z-phase particles than pure Ta-based Z-phase particles [24]. However, Ta and Nb behave more alike, compared with V in these steels. This is shown by the fact that Z-phase of the types Cr(V,Ta)N and Cr(V,Nb)N are similar to each other [18]. Furthermore, the morphology of Ta-based Z-phase is rather different from the V-based one. Instead of the thin faceted plates of the V-based Z-phase [28], Ta-based appear more like Nb-based Z-phase, that is found in austenitic steels. These particles are generally smaller and tetragonal in shape [29].

In 9–12% Cr steels, with a high Cr content and a relatively high C content, MX particles were found, with a composition of either Ta(C,N) or pure TaN. Z-phase transformation from Ta(C,N) particles, occurs through in-diffusion of Cr and out-diffusion of C. For pure TaN particles, only in-diffusion of Cr is needed. Thus, the transformation of Z-phase from TaN particles is quicker, than it is from Ta(C,N) particles. Z-phase and Ta(C,N) particles can co-exist, which suggest that Z-phase transform from Ta(C,N) particles, rather than direct formation on their own. This would mean that Z-phase form at the expense of Ta(C,N) particles, which would decrease the precipitation strengthening that Ta(C,N) provides [23]. However, if the newly formed Z-phase coarsen slowly, they also provide precipitation strengthening.

3 Methods

In the following chapter, methods used for the investigation of test material ZL3 are presented. Firstly, the material and the heat treatment are described, followed by the mechanical testing methods. Furthermore, the techniques of Light optical microscopy (LOM), Scanning electron microscopy (SEM) and Transmission electron microscopy (TEM) are described, together with the sample preparation for these techniques.

3.1 Material

The material investigated in this study is called ZL3. It is a new Z-phase strengthened 12% Cr steel. The chemical composition of ZL3 is shown in *Table 3.1*.

Table 3.1 The chemical composition of ZL3 steel.

	Fe	C	Mn	Si	Cr	Ni	W	Co	Cu	B	N	Ta	Mo
wt%	bal.	0.06	0.21	0.31	12.1	0.19	2.47	3.5	1.95	0.006	0.049	0.36	0.01

The heat treatment of ZL3 was performed in several steps, which can be seen in *Figure 3.1*. The first step is austenitization at 1150°C for 1 hour. In this step, parts of the primary particles were dissolved into solid solution. The material was then air quenched to obtain a martensitic structure. After this, two step tempering treatment was performed, to reduce residual stresses and to form secondary precipitates. The first tempering treatment was done at 650°C for 6 hours. The second tempering treatment have two versions, either at 700°C or 740°C for 6 hours. It resulted in two versions of steels with either a High Yield strength (HY) or Low Yield strength (LY), and thus the two steels are hereafter referred to as ZL3 HY and ZL3 LY, respectively.

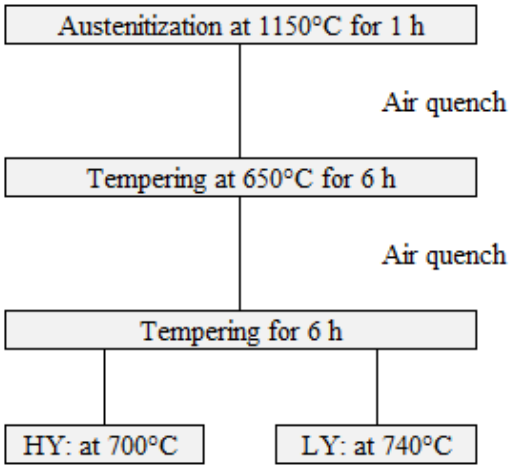

Figure 3.1: Flow chart of heat treatment of the test material.

3.2 Creep and mechanical testing

Creep testing and mechanical testing was carried out at Siemens Industrial Turbomachinery in Finspång. From each version, HY and LY, individual specimens were prepared.

3.2.1 Creep testing

Creep testing was done at 650°C with a load of 120 MPa, 100 MPa and 80 MPa. Tensile, hardness, and impact testing, were done for ageing times of 3 000 h, 10 000 h and 30 307 h at 650°C. The size of the test bars was 35x35 mm. The aged blanks were 65 mm long.

3.2.2 Hardness testing

Hardness is defined as the materials machinability and resistance to scratching or penetration. Often hardness is used to evaluate tempering or hardening effects during heat treatment or cold forming [32]. One common method of hardness testing is the Vickers hardness test method, where a diamond indenter is used. The diamond indenter is in the form of pyramid and it is forced into the material. The two diagonals of the square shape left in the material is measured and a HV number is given. In the case of HV30, HV is the hardness symbol and 30 means that the forced used is 30 kgf [33].

For test material ZL3 the standard DIN EN ISO 6507-1:2018 [33] for Vickers hardness was used. The hardness testing was done on the side of the impact test samples for each ageing time. Beforehand the samples were milled and polished.

3.2.3 Tensile testing

Tensile testing is done to determine mechanical properties at room temperature. Example of mechanical properties are the tensile strength (R_m), the proof (yield) strength ($R_{p0.2}$), percentage after fracture (A) and percentage reduction area (Z). The test piece is usually obtained by machining samples from a product, a pressed blank or from casting. The cross-section of specimen is either of circular, rectangular or some other uniform shape. The specimen is placed in the testing machine, where increasing load is applied until fracture [32][34]. For test material ZL3, tensile testing at room temperature, was done in accordance with standard DIN EN ISO 6892-1:2017 [34].

3.2.4 Impact testing

Impact tests are done to measure the energy absorbed by the material under shock loads. The test is done by a swing pendulum that is released from a fixed high and hit the specimen with a single blow. The angel, which the pendulum reaches after the impact, is measured and indicates the energy that been absorbed, which corresponds to the materials toughness [32,35].

Impact testing of test material ZL3 was done according to standard DIN EN ISO 148–1:2017 [35] for the Charpy pendulum impact test method. The standard test piece was 55 mm long with 10x10 mm cross section with a 2 mm deep V-notch and the test was carried out at room temperature. The average absorbed energy from three specimens was reported.

3.3 Light optical microscopy

A light optical microscope (LOM) uses reflected light to illuminate the specimen. With a combination of different lenses, fine details of the specimen's microstructure can be

shown at a typical magnification between 50x to 2000x. While LOM lacks the resolution of SEM and TEM and the depth of field of SEM, the advantage is a quick visual observation of the bulk material's surface structure of a large area. Thus, LOM is an important complement to SEM and TEM. During examination of a metal it also often standard to start from a lower magnification and resolution and progressively go higher [36].

3.4 Scanning electron microscopy

A scanning electron microscope (SEM) analyses the specimen on a micrometre or sub-micrometre scale, with a resolution up to 1 nm and a depth of field greater than that of an optical microscope. Both low and high magnification is possible. One of the major parts of a SEM is the electron column, where the electron gun emits a stable source of electrons. The electrons get accelerated to an energy normally in the range of 0.1–30 keV and travel through electromagnetic lenses, which create a focused electron beam. The electron gun used nowadays is often a field-emission gun (FEG-SEM). The other major part of a SEM is the control console, which controls the beam through a computer and a display [37].

When the electrons emitted from the electron gun reach the specimen, the electrons reach different depths in the specimen, known as the interaction volume. From the interaction volume different signals are sent back and caught by different detectors. The major signals are: secondary electrons (SE), backscattered electrons (BSE) and characteristic X-rays. SEs are emitted with an energy less than 50 eV and come from near the surface of the interaction volume. SEs provide topographical images with a large depth of field, which gives a three dimensional impression. Simultaneously, BSEs are emitted with an energy close to that of the electrons from the electron gun. With BSE it is possible to get information on the specimen's chemical composition, since the efficiency of generating BSEs depends on the atomic number. An atom with a higher atom number will appear brighter than an atom with a lower atom number [37]. Finally, there are characteristic X-rays, which can be used in both SEM and TEM, and are described further in section 3.6.

Images were taken using both SEs and BSEs, in ZEISS-LEO 1550 Schottky Field Emission SEM and Philips XL30 ESEM, to get an overview, as well as a close-up, of the specimen's microstructure.

3.5 Transmission electron microscopy

A transmission electron microscope (TEM) consists of an electron gun, several electromagnetic lenses, and a viewing screen. In a TEM, electrons transmit through an ultra-thin specimen and create images with a resolution below 0.1 nm (1 Å). Ultra-thin in this case means electron transparent, which is needed for the electrons to pass through the specimen. To create these ultra-thin specimens the sample preparation for TEM is vital, and also one of the major obstacles of using TEM [38]. Techniques often applied are creation of extractive carbon replicas (for particles in materials), cutting and electropolishing (for bulk conductive materials) and ion polishing. The first two methods are described more closely in Appendix 1 and sub-section 3.8.2, respectively.

Unlike in SEM, the electrons that pass through the specimen are caught by different detectors. Like in SEM, characteristic X-rays are caught by EDX. Thus, information of the chemistry of the specimen is provided. Unlike in SEM, EDX can be done at much higher resolution, at a nanoscale. However, in TEM only small areas can be analysed at the same time and thus the sampling in TEM is less than it is in SEM or in LOM. It is therefore recommended to start from a lower magnification in LOM or SEM to get a good sampling of the specimen, and then continue to higher magnification and resolution in TEM [38].

Analyses were performed using FEI Tecnai T20, which is a TEM/STEM with a LaB_6 filament, at 200 kV.

3.6 Energy dispersive X-ray spectroscopy

When the electron beam, in SEM or TEM, interacts with atoms in the specimen, an electron in the inner shell of an atom can be kicked out. The energy of the atom, thus, increases. An electron from the outer shell falls into the empty position in the inner shell, thus, lower the energy of the atom. The energy difference between these two levels results in radiation of characteristic X-rays [39]. The difference in energies between any two levels are unique for each element. This means that by comparing the energy of X-rays to the characteristic energies of known elements, the specimen's composition can be determined [1,39].

The X-rays are sampled by an energy dispersive X-ray spectroscopy (EDX) detector. Analysis can, for example, be done by spot analysis or mapping. Spot analysis gives the composition of chosen spots and is convenient for quick analyses. EDX mapping gives elemental maps of the material.

3.7 Atom probe tomography

Atom probe tomography (ATP) is a method there the chemical composition and reconstruction of individual atoms are possible. The samples used are very sharp and fine needles, with a tip radius less than 50 nm. The atoms from the tip get ionized under a very high electrical field (in the order of 10^{10} V/m). The time-of-flight of ions is unique for each ion and therefore the chemical composition can be decided. Normally the evaporation is induced by high voltage pulsing or by laser pulsing [40].

3.8 Sample preparation

To study samples in various microscopes, sample preparation is necessary. Sub-section 3.8.1 describe sample preparation for LOM and SEM. Sub-section 3.8.2 describe the process of preparing self-supporting samples for TEM. For carbon replicas used in TEM, see Appendix 1.

3.8.1 Mounted samples

To study the material with LOM and SEM, the samples were first cut and mounted in Bakelite resin. Thereafter, they were mechanically grinded with SiC paper with a grit of 500 µm at a force of 30 N for 5 minutes. Samples were then polished with MD-Largo

with a suspension of DiaPro Allegro/Largo 9 µm, MD-DAC with DiaPro Dac 3 µm and MD-Nap with DiaPro Nap-B 1 µm.
For the microstructure to appear, the samples were etched with Villela's reagent, which consists of:

- 9 ml glycerol
- 9 ml nitric acid
- 6 ml hydrochloric acid

Samples were etched for 15-20 seconds and then washed with ethanol and water. It is important to note that this etchant also removes Cu particles and leave behind holes in the matrix.

3.8.2 Self-supporting TEM samples

Preparation of self-supporting TEM samples begins with bulk material. Material pieces were cut to a thickness of 300 µm and then grinded down to 50 µm. From this piece, disks were stamped out, with a diameter of 3 mm. The disks were electropolished using a Struers Tenupol Twin Jet electropolisher, with an electrolyte of 10% perchloric acid and 90% methanol at -35°C. Samples were electropolished until a tiny hole was formed. The area around the hole is electron transparent, which is needed for the electrons to pass through the specimen in the TEM.

This method of preparing samples for TEM is robust and the particles preserve their direct relationship with the matrix. However, there are magnetic interference from the specimen in the TEM.

3.9 Measurement of average prior austenite grain size

To determine the average prior austenite grain size, ASTM E112-13 [41], specifically the Heyn Lineal Intercept Procedure, was used. Five random fields of the specimen were selected. For each field seven straight lines of equal length were drawn in random orientation. The intersections between lines and grain boundaries were counted. Each intersection was counted for 1 point each. If the end of the line fell on a grain boundary it was counted as ½, while if an intersection occurred at a triple point was counted as 1½. Together all the seven lines should reach at least 50 intercepts, meaning that the magnification should be sufficiently low and the lines should be sufficiently long to reach this amount [41].

The total number of intersections from all lines were counted and the average lineal intercept length, $\bar{l}$ was calculated according to equation 3.1, there L_T is the total length of the lines, P is the number of intersections in total and M is the magnification.

$$\bar{l}_i = \frac{L_T}{PM} \tag{3.1}$$

The mean value of $\bar{l}$ was calculated with equation 3.2, and was then used to calculate the standard deviation, s, see equation 3.3. n is the number of randomly selected fields measured.

$$\bar{l} = \frac{\sum l_i}{n} \tag{3.2}$$

$$s = \left[\frac{\sum \left(l_i - \bar{l}\right)^2}{n-1}\right]^{1/2} \tag{3.3}$$

3.10 Analysis of boron nitride particles

Boron nitride particles were studied and documented by using BSE in FEG-SEM. 50 images were taken for each sample, 10 from each corner and 10 in the middle, which can be seen in *Figure 3.2*.

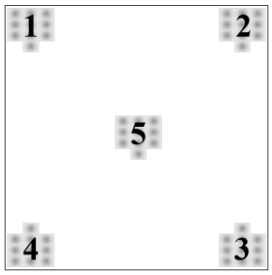

Figure 3.2 Schematic drawing of the areas at which images are taken from each sample.

Images taken with BSE gives a chemical composition contrast. BN particles have a much lower average atom number than the Fe-Cr matrix have, which means they appear darker. This can be seen in *Figure 3.3 a)*, there the BN particles are pointed out with arrows. Much smaller black dots can also be seen. These are the holes left in the matrix, when Cu particles were removed during etching.

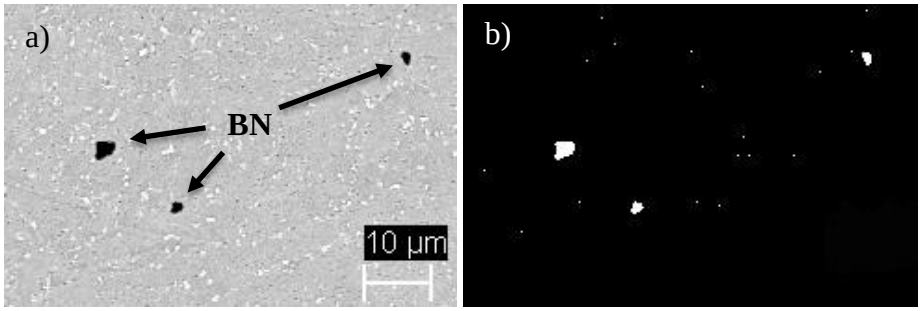

Figure 3.3 SEM micrograph, showing boron nitride particles. a) the original image and b) the image after segmentation manipulation in ImageJ.

Images then went on to be analysed using the image processing program ImageJ, which is designed for scientific multidimensional images. The grey scale threshold was set first, so only the particles with the "right" contrasts were recognised, and then turned the image into completely black or white areas. The previously black BN particles can now be seen as three large white dots in *Figure 3.3 b)*. Using the function "Analyse Particles" in ImageJ gives a summary of all the particles. The summary consists of the area of each particle and the total area fraction of precipitation for each image. By adjusting the size, to only include particles between 0.4 µm and infinity, the holes from Cu particles was not taken in to account in the summary. Thus, only results of the BN particles are given.

3.11 Analysis of secondary particles

Secondary particles were studied in TEM. Each particle was analysed with EDX, to get its chemical composition. Images were then analysed with Image J, in a similar way as the boron nitride particles, which is described in sub-section 3.10. However, the contrast between particles and matrix, and the interference of thickness contour bands and local strain contrast, which can be seen in the TEM, meant that the threshold to recognise the "right" contrasts were not as straight forward. Instead particles were "filled in" and contrasts that were part of the matrix were "erased". This resulted in images like *Figure 3.4*, which show an image of sample ZL3 LY aged for 30 307 hours, both in its original state and after manipulation in ImageJ.

Using the function "Analyse Particles" in ImageJ gave a list of the area of each particle, beginning with the particle that appear at the top and continuing the list in order of appearance of the particles. The result was then matched with corresponding result from EDX spot analysis, to find out which area belonged to which type of particle.

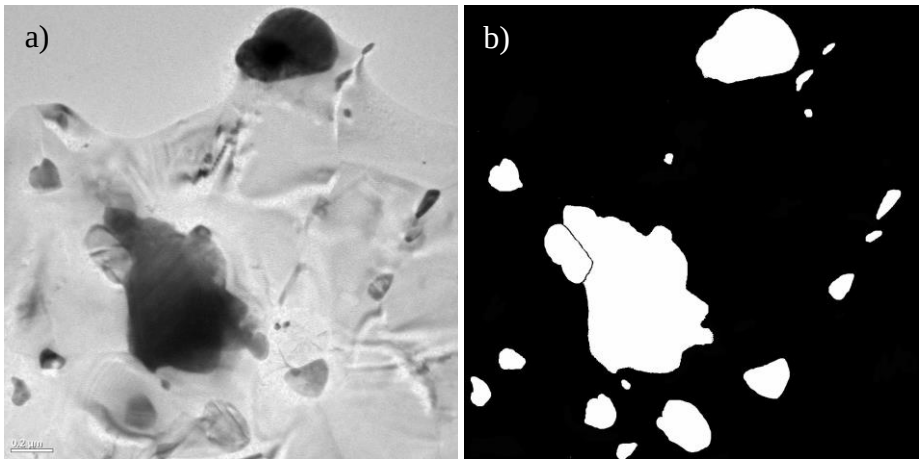

Figure 3.4 TEM micrograph. a) original image, and b) the image after manipulation in ImageJ.

4 Results

In the following chapter the results from the investigation of test material ZL3 will be presented. Creep testing and mechanical testing done at Siemens Industrial Turbomachinery AB in Finspång is presented first. The mechanical testing is shown in the form of different diagrams showing the hardness, the yield strength, the ultimate tensile strength and the impact toughness. Then the size of the pre-austenite grains is presented, followed by primary and secondary particles, respectively.

4.1 Creep properties

Creep curves for ZL3 at 650°C, see *Figure 4.1*, show that HY perform better than LY at all applied stresses. Nonetheless, it can also be seen that the creep curves for HY are much steeper in the middle part of creep than in LY. Additionally, in creep-resistant 9–12% Cr steels, creep curves tend to directly continue to tertiary creep from primary creep [1]. The same behaviour is seen in ZL3.

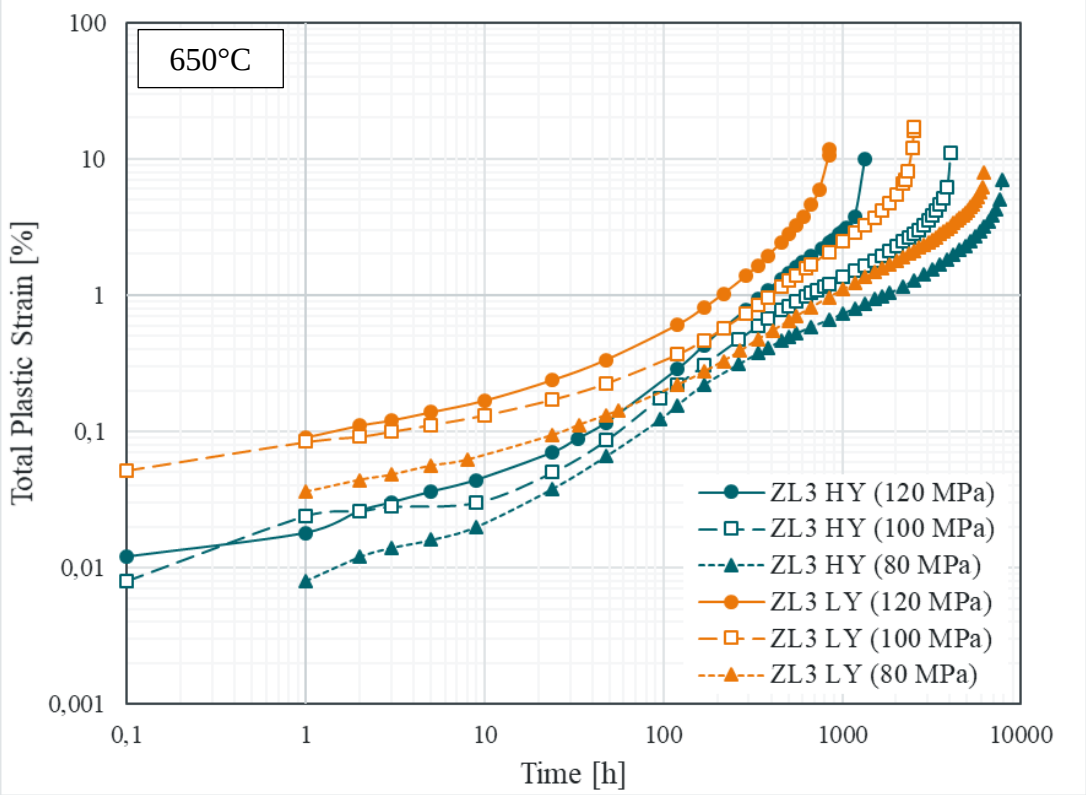

Figure 4.1 Creep curves for ZL3 HY and ZL3 LY at 650°C for 120 MPa, 100 MPa and 80 MPa.

Creep rupture curves for ZL3 HY and LY at 650°C, see *Figure 4.2*, show that HY performs better than LY. Creep rupture curves after 10 000 hours are interesting to check, however, so far there is no creep rupture data beyond 8 000 hours for ZL3 at 650°C.

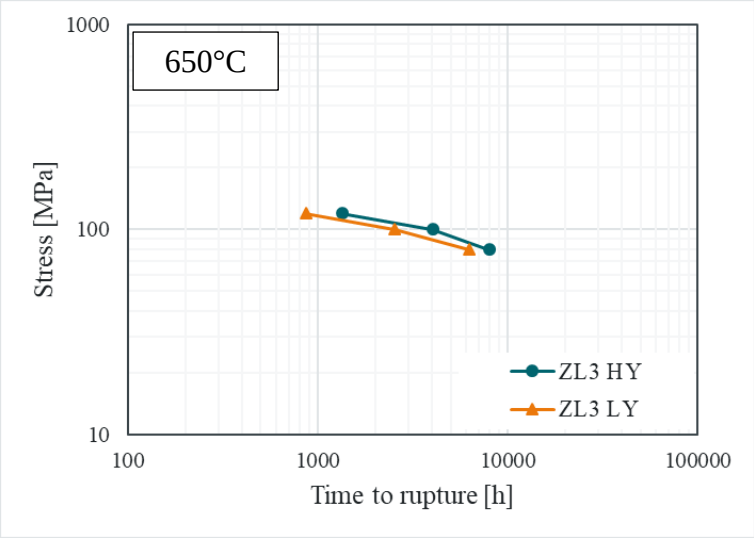

Figure 4.2 Creep rupture curves for ZL3 HY and LY at 650°C.

4.2 Mechanical properties

In *Figure 4.3*, the result of the hardness testing can be seen. ZL3 HY starts out as the hardest material at 322 HV30, while ZL3 LY, in comparison, starts out at 267 HV30. With ageing time, the hardness decreases for both HY and LY, and after 30 307 hours of ageing the curves almost coverage, with hardness values of 211 HV30 and 208 HV30, respectively.

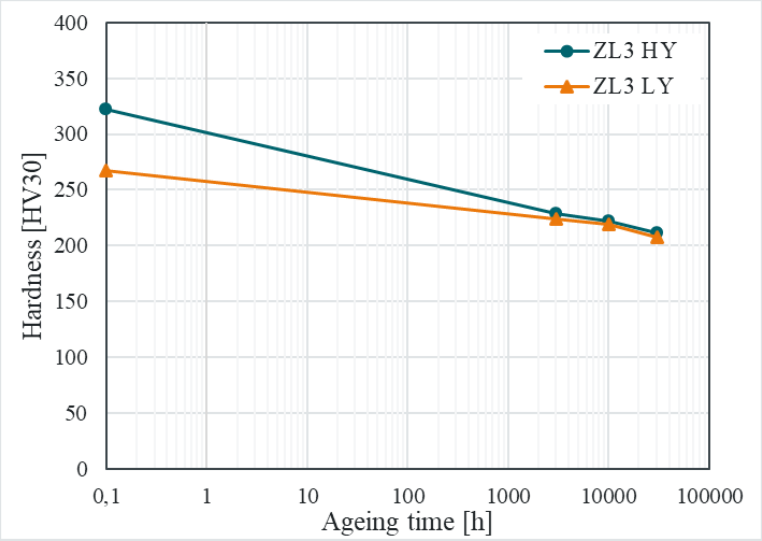

Figure 4.3 Hardness-Time diagram for ZL3 HY and ZL3 LY. The two curves coverage to almost one point after 30 307 hours.

In *Figure 4.4*, the yield strength ($R_{p0.2}$) and the ultimate tensile strength (R_m), for ZL3 HY and LY is presented. For HY at its virgin state, the yield strength is 870 MPa and the ultimate tensile strength is 963 MPa. Meanwhile for LY at its virgin state, the yield strength is 686 MPa and the ultimate tensile strength is 794 MPa. In line with the result for hardness, the curves for yield strength and the curves for ultimate tensile strength, converge with ageing time. After, 30 307 hours, the yield strength are 493 MPa and 472 MPa, for HY and LY, respectively, and 660 MPa and 647 MPa, for HY and LY, respectively.

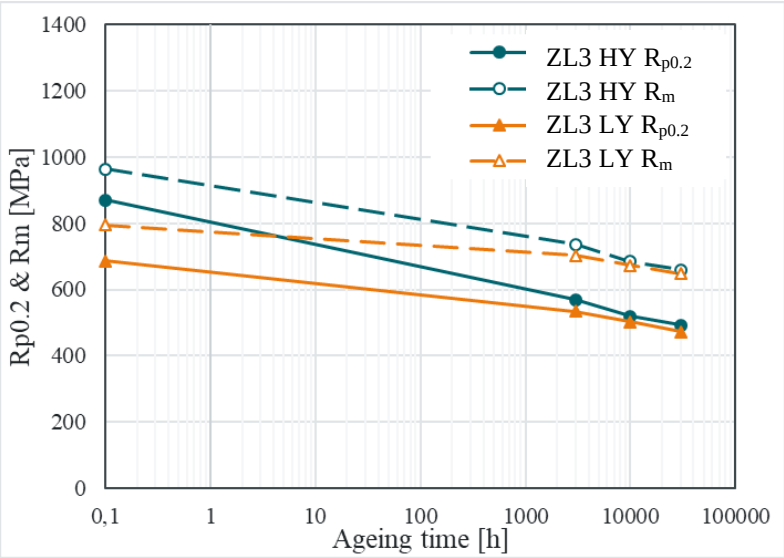

Figure 4.4 Strength-Time diagram for ZL3 HY and ZL3 LY. The two pairs of curves converge correspondingly after 30 307 hours.

For impact toughness, see *Figure 4.5*, the samples roughly follow the same pattern. At their virgin state, absorbed energy for ZL3 HY was 33 J and for ZL3 LY was 100 J. While the curves cross each other at 3 000 hours of ageing, they then come closer at 30 307 of ageing. After 30 307 hours, the impact values are 57 J and 52.5 J, for HY and LY, respectively

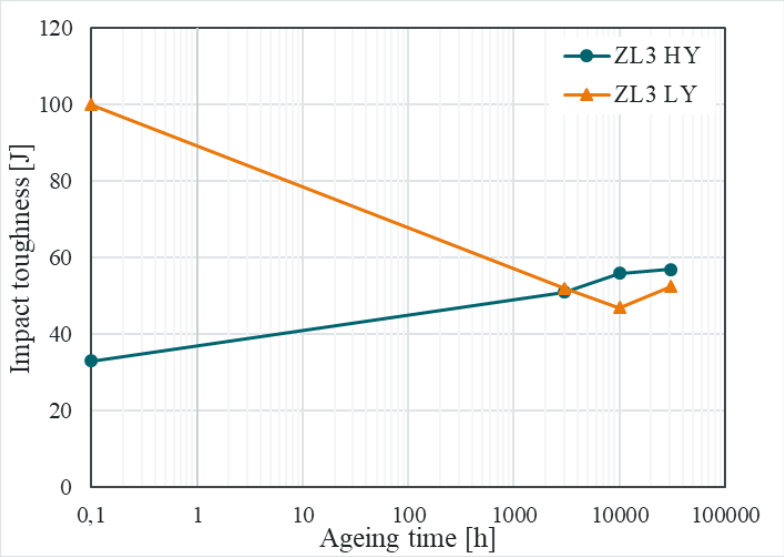

Figure 4.5 Impact toughness-Time diagram for ZL3 HY and ZL3 LY.

4.3 Prior austenite grain size

Using ASTM E112-13 to determine the average prior austenite grain size, gave ZL3 HY and Zl3 LY a prior austenite grain size of 59±4 µm and 61±3 µm, respectively. The result can be seen in *Table 4.1*. The prior austenite grain size only differs slightly for the two tempering temperatures, HY and LY, and within measurement deviation. Thus, the tempering temperature does not have a significant impact on the prior austenite grain size.

Table 4.1 The average prior austenite grain size and the standard deviation of ZL3 HY and ZL3 LY.

Sample	Average grain size [µm]	Standard deviation
ZL3 HY	59	4
ZL3 LY	61	3

4.4 Primary precipitates

For each tempering temperature, HY and LY, four states were studied in the SEM. These were the virgin state, 3 000 hours of ageing, 10 000 hours of ageing and 30 307 hours of ageing. An overview of the microstructure in SEM, for the virgin state and 30 307 hours of ageing, can be seen in *Figure 4.6*. With these SEM images, only primary particles could be studied. The primary particles are boron nitride and primary MX, which are describe more in sub-sections 4.4.1 and 4.4.2 respectively.

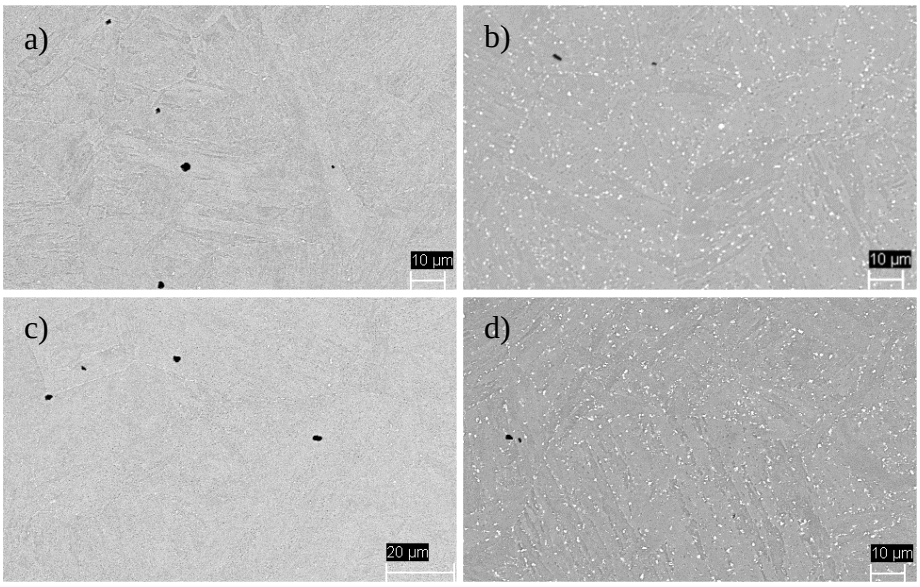

Figure 4.6 SEM micrographs showing the microstructure of a) ZL3 HY in the virgin state, b) ZL3 HY for 30 307 h of ageing, c) ZL3 LY in the virgin state, and d) ZL3 LY for 30 307 h of ageing.

4.4.1 Boron nitride particles

SEM micrographs showed that the BN particles seem to be larger in the virgin state compared to the aged samples. To confirm this, 50 images were taken for each sample, 10 in each corner and 10 in the middle, which can be seen in *Figure 3.2*. Each area, which sets of 10 images were taken, are referred to as sites. The area fraction of BN particles for each site in each sample, can be seen in *Figure 4.7*. For each sample 219±35 particles were studied.

The results of the different sites in these samples, show that scattering of the area fraction of BN particles exists even in the same sample. However, the previous observation that BN particles seem to be larger in the virgin state compared to the aged samples, were also observed here. While the aged samples average area fraction is between 0.016-0.021%, the virgin state for HY is 0.043% and for LY is 0.065%.

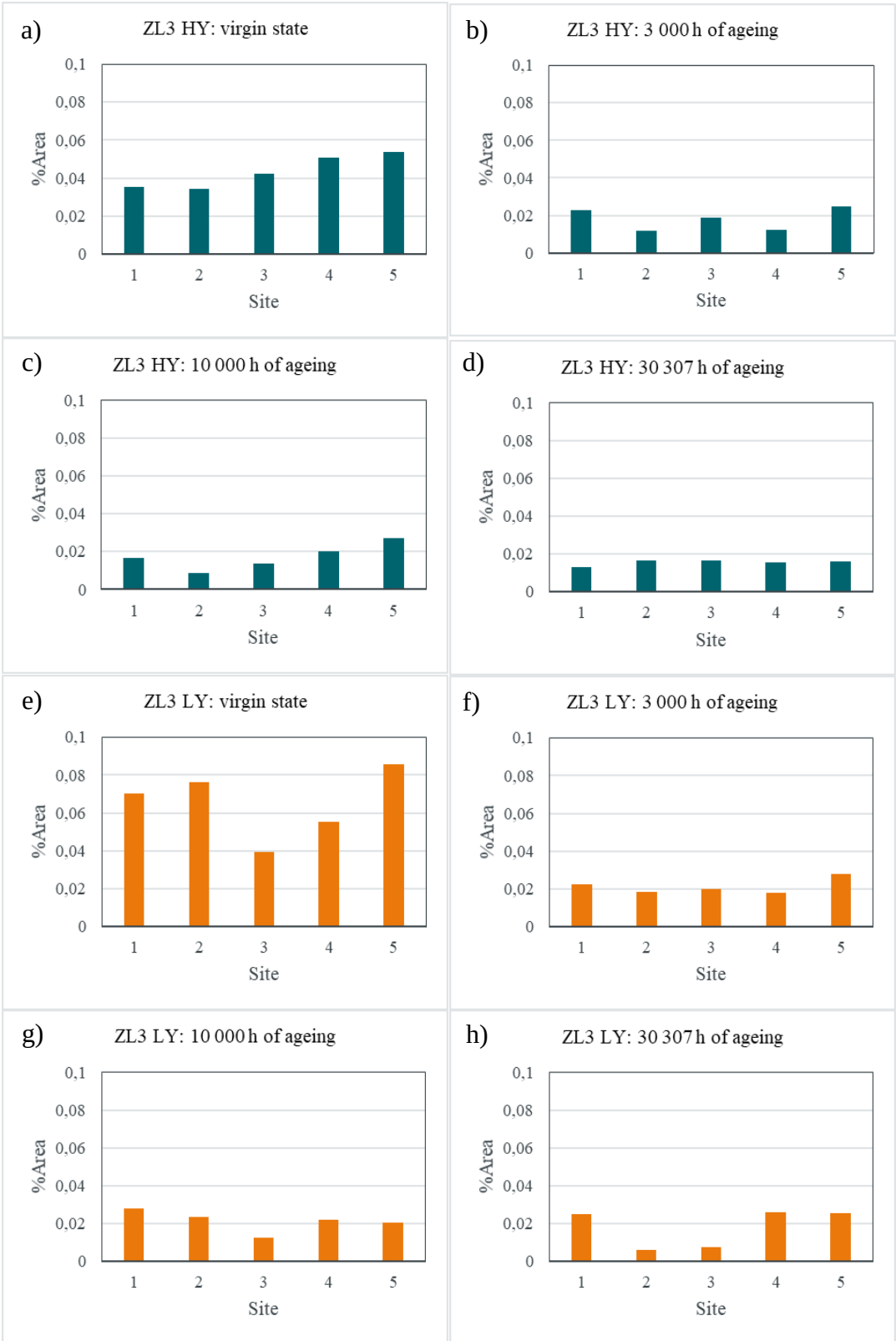

Figure 4.7 Area fraction of boron nitride particles at different sites for a) ZL3 HY virgin steel, b) ZL3 HY for 3 000 h of ageing, c) ZL3 HY for 10 000 h of ageing, d) ZL3 HY for 30 307 h of ageing, e) ZL3 LY virgin steel, f) ZL3 LY for 3 000 h of ageing, g) ZL3 LY for 10 000 h of ageing, and h) ZL3 LY for 30 307 h of ageing.

Since BN particles are thermodynamically stable at 650°C, it is very unlikely that there is a correlation between the area fraction of it with the ageing time. Therefore, for each tempering temperature, HY and LY, two new virgin samples (HY0a, HY0b, LY0a and LY0b) were analysed to get better statistics. The area fraction of BN particles of these samples, together with the original samples (HY0 and LY0) can be seen in *Figure 4.8*.

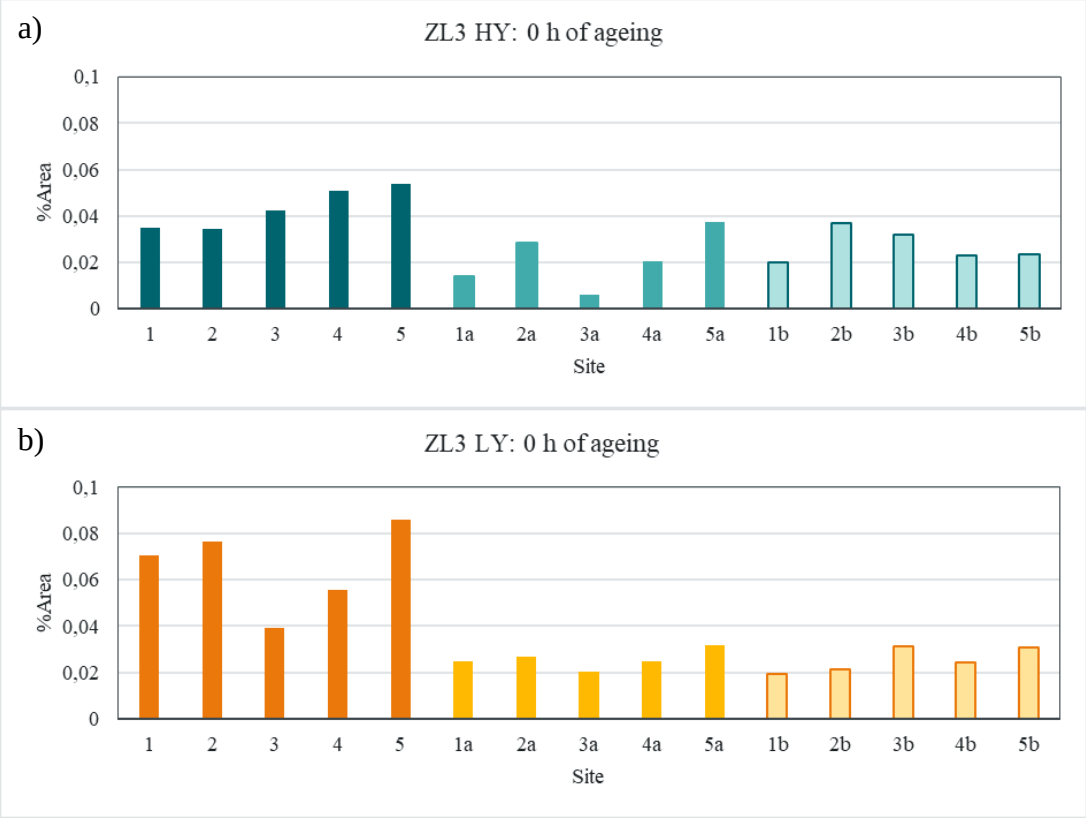

Figure 4.8 Comparison of area fraction of boron nitride particles at different sites for a) ZL3 HY and b) ZL3 LY in their virgin state.

The result of the newly added samples show that the area fraction of BN particles is much lower compared to the first measured samples. However, the scattering of area fraction of BN particles, seen in *Figure 4.9*, show that the area fraction of the new samples still is larger than that of the aged samples. For the new samples, the average area fraction for HY is between 0.021-0.027% and for LY is 0.025%. The reason behind this is likely that there is an overall uneven distribution of BN particles in the original bar, from which the samples were taken.

The appearance of BN particles was found to be dependent on the hot rolling direction. In *Figure 4.10 b)*, ZL3 HY0b is shown. In this sample the BN particles are small and round. This is also the appearance BN particles shown in the other samples. Meanwhile in sample ZL3 HY0a, seen in *Figure 4.10 a)*, the particles are big and elongated in the rolling direction. However, a large number of images taken of ZL3 HY0a do not have any particles at all. Therefore, the area fraction of BN particles does not seem to be affected by the hot rolling direction, since the average area fraction for HY0a is 0.021% and for HY0b is 0.027%. These area fractions are in line with the other samples, which can be seen in *Figure 4.9*.

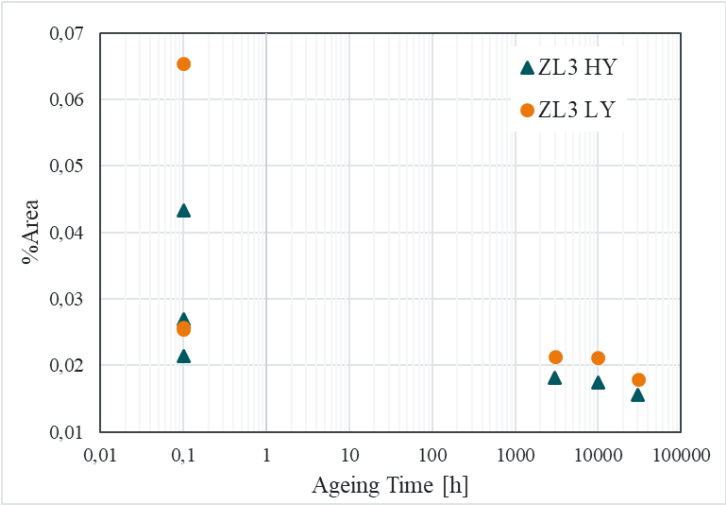

Figure 4.9 Scattering of area fraction of BN particles in different samples.

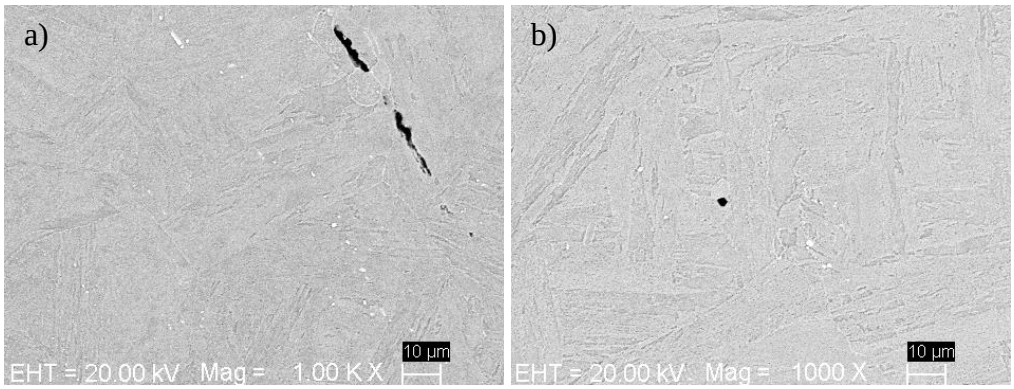

Figure 4.10 SEM micrographs showing the microstructure of BN particles in samples with different orientation relative to the rolling direction a) ZL3 HY0a and b) ZL3 HY0b.

4.4.2 MX

Primary MX particles that exist from the austenitization stage, are large and do not transform into Z-phase during ageing. In *Figure 4.11 a)*, which is of ZL3 HY in the virgin state, several MX particles together with one large boron nitride particle can be seen. For ZL3 HY which have been aged for 30 307 hours, see *Figure 4.11 b)*, one MX particle growing on a large TaO particle and several Laves particles is shown. The same types of particles were seen for the different ageing times in sample ZL3 LY as well.

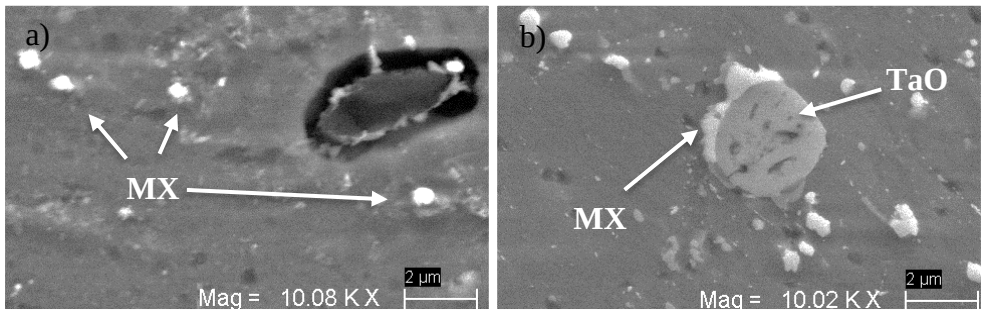

Figure 4.11 SEM micrography showing primary MX particles in sample ZL3 HY for a) the virgin state and b) 30 307 h of ageing.

In test material ZL3 which contains Ta, but no V and Nb, most of the primary MX particles are of the type TaC. The Ta and C peaks in *Figure 4.12*, show the spectrum of a TaC particle in the sample ZL3 HY in the virgin state. Peaks of Fe and Cr can also be seen, which come from the matrix.

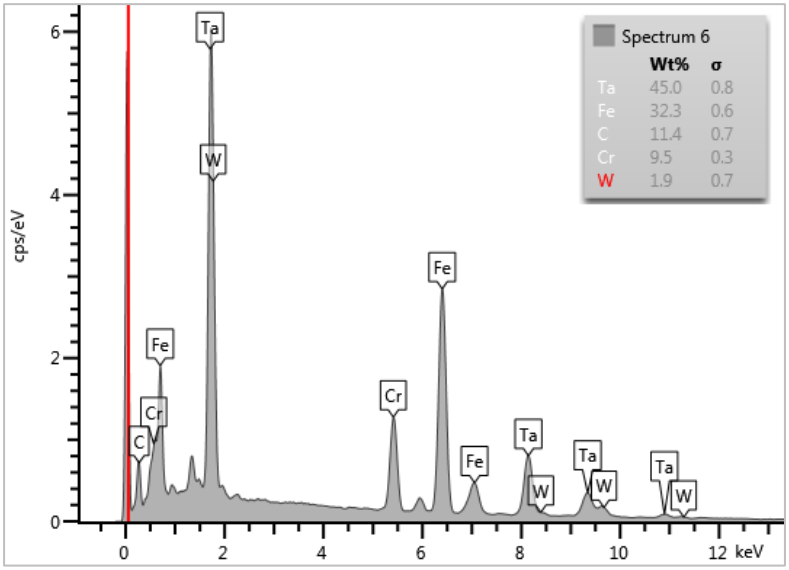

Figure 4.12 EDX spot analysis taken from ZL3 HY in the virgin state, showing the spectra of a primary MX particle.

In the TEM, primary and secondary MX particles can be distinguished by the primary MX particles large size and round appearance. An example of a primary MX particle in TEM can be seen in *Figure 4.13*, which is taken from sample ZL3 LY that has been aged for 30 307 hours. Primary MX particles have also been found in other studied samples.

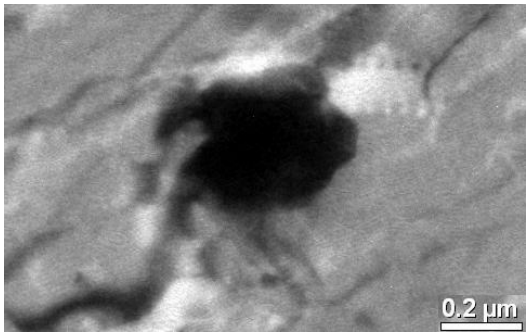

Figure 4.13 TEM micrograph showing a primary MX particle in sample ZL3 LY aged for 30 307 h.

4.5 Secondary precipitates

Secondary particles that were ready to be analysed in the SEM were Laves-phase. Therefore, Laves-phase were studied for all four states (virgin, 3 000 hours of ageing, 10 000 hours of ageing and 30 307 hours of ageing) for materials with both tempering temperatures, HY and LY. For the remaining particles, which are too small or give too little contrast for analyses in the SEM, analyses were done in the TEM. However, due to time constraint, only two states (3 000 hours of ageing and 30 307 hours of ageing) for both tempering temperatures, were studied in the TEM.

Particles that were found with the TEM were $M_{23}C_6$, Laves-phase, MX, Z-phase, and hybrid particles referred to Z/MX, which have a composition somewhere in between MX and Z-phase. M_2X particles of the type Cr_2N were also found, but only two of them. These two particles can be seen in *Figure 4.14*, which are from sample ZL3 LY aged for 30 307 hours. A deeper analysis of $M_{23}C_6$, Laves-phase, Z-phase and MX, are reported in sub-sections 4.5.1–4.5.3.

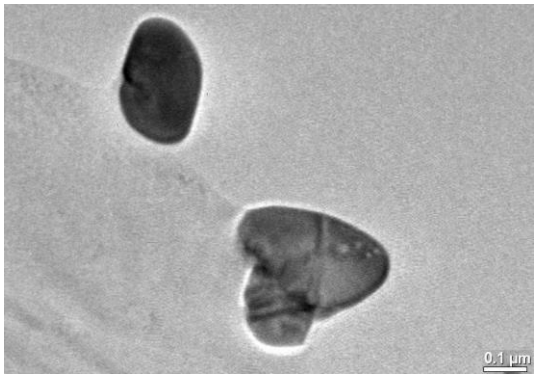

Figure 4.14 TEM micrograph showing two large M_2X particles in the sample ZL3 LY aged for 30 307 h.

4.5.1 $M_{23}C_6$

$M_{23}C_6$ particles are beneficial carbides in 12% Cr steel. In ZL3, $M_{23}C_6$ particles are of the type $Cr_{23}C_6$, though some small amount of the Cr content can be replaced with Fe and Ta. $M_{23}C_6$ particles occur both as single individual particles, as well as clusters of particles, see *Figure 4.15*. While *Figure 4.15* show material ZL3 LY aged for 3 000 hours, the same behaviour was found in all the studied samples.

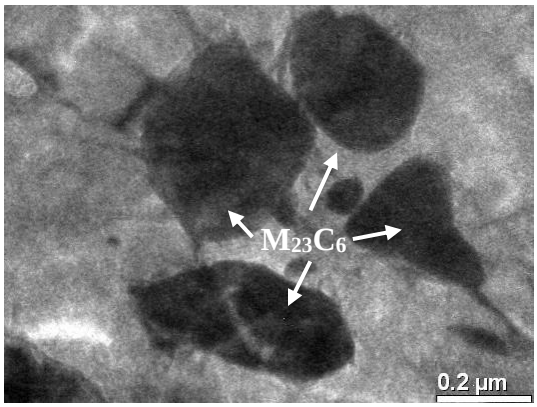

Figure 4.15 TEM micrography showing a cluster of large $M_{23}C_6$ particles in sample ZL3 LY aged for 3 000 h.

The area distribution of $M_{23}C_6$ particles are presented in *Figure 4.16*. For ZL3 HY that is aged for 3 000 hours, the particles are mostly distributed around the lower end of the x-axis. This behaviour mostly remains at 30 307 hours of ageing, with a few particles that are slightly bigger. In contrast, for ZL3 LY that is aged for 3 000 hours, the particles are more distributed in the middle of the x-axis. After 30 307 hours of ageing some of the particles have grown significantly larger, reaching beyond 0.1 μm^2.

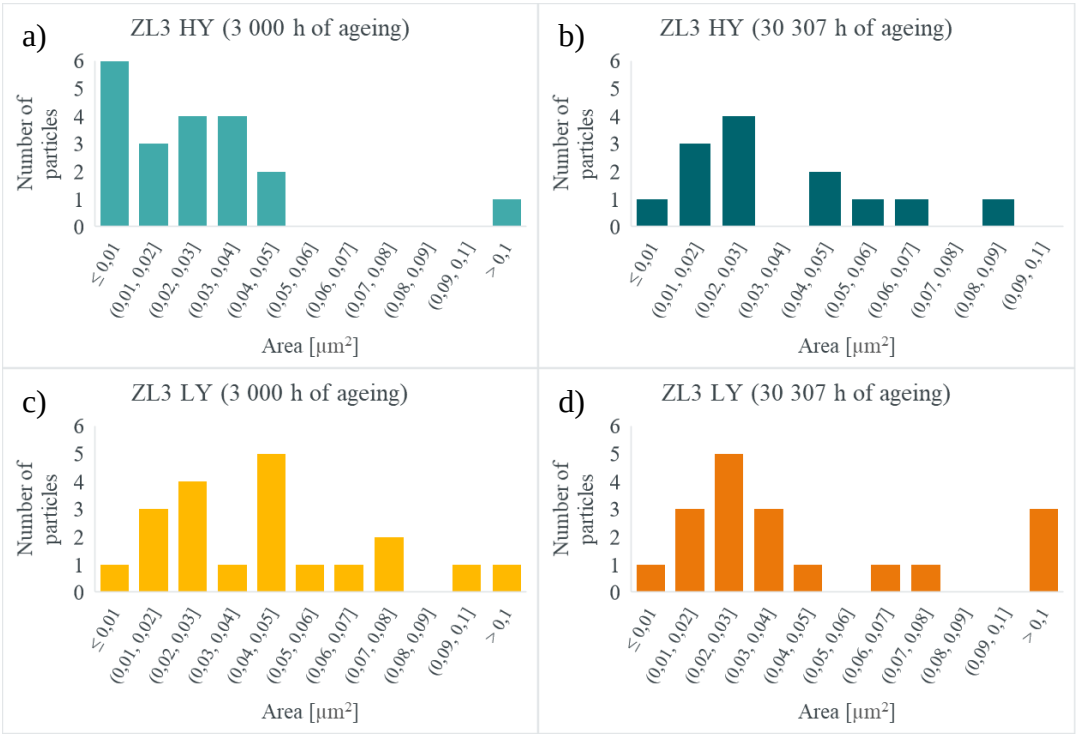

Figure 4.16 Area distribution of $M_{23}C_6$ particles in a) ZL3 HY for 3 000 h of ageing, b) ZL3 HY for 30 307 h of ageing, c) ZL3 LY for 3 000 h of ageing, and d) ZL3 LY for 30 307 h of ageing.

The average particle area of $M_{23}C_6$ particles, with standards deviation, is shown in *Table 4.2*. It can be seen that after 3 000 hours of ageing particles in HY is on average 0.026 µm^2 and increase to 0.034 µm^2 after 30 307 hours of ageing. Meanwhile in LY the average area is 0.044 µm^2 after 3 000 hours of ageing and 0.054 µm^2 after 30 307 hours of ageing. Thus, the particles are on average smaller in HY compared to LY. However, in both cases the particles grow very slowly, meaning that tempering temperature and ageing time only slightly affect the more or less stable $M_{23}C_6$ particles.

Table 4.2 The average particle area and the standards deviation for $M_{23}C_6$ particles depending on tempering temperature (HY and LY) and ageing time (3 000 hours of ageing and 30 307 hours of ageing).

	ZL3 HY		ZL3 LY	
Ageing time [h]	Area [µm^2]	Standard deviation	Area [µm^2]	Standard deviation
3 000	0.026	0.022	0.044	0.027
30 307	0.034	0.021	0.054	0.052

4.5.2 Laves-phase

Laves-phase grow significantly with ageing time and can be analysed in the SEM. In *Figure 4.17* sample ZL3 HY is shown for the four states: virgin, 3 000 hours of ageing, 10 000 hours of ageing and 30 307 hours of ageing. In the virgin state, there are very few Laves particles present. In the sample aged for 3 000 hours, the Laves particles appear small and needle like. Finally, in the samples aged for 10 000 and 30 307 hours they have grown significantly larger and are often irregular in shape. The same behaviour was observed in the sample ZL3 LY, see *Figure 4.18*. The difference in

Laves-phase between the two tempering temperatures, HY and LY, was not analysed in the SEM quantitively, since after longer aging time it is difficult to distinguish between MX/Z-phase and Laves phase, which all show similar contrast.

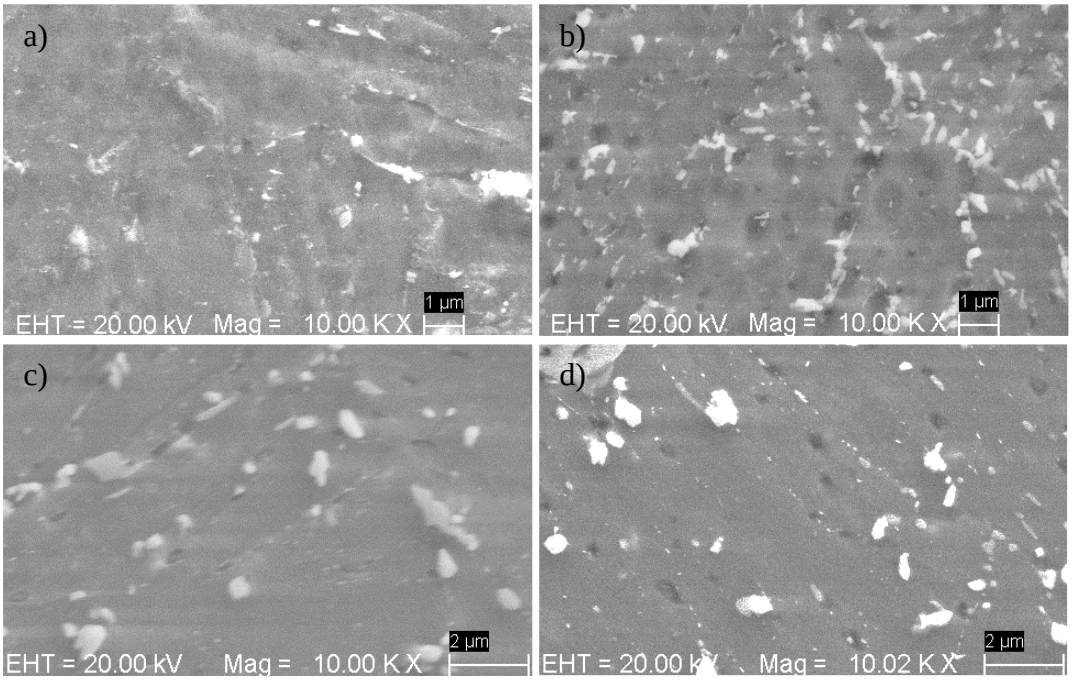

Figure 4.17 SEM micrograph showing the microstructure of ZL3 HY in a) the virgin state, b) 3 000 h of ageing, c) 10 000 h of ageing, and d) 30 307 h of ageing.

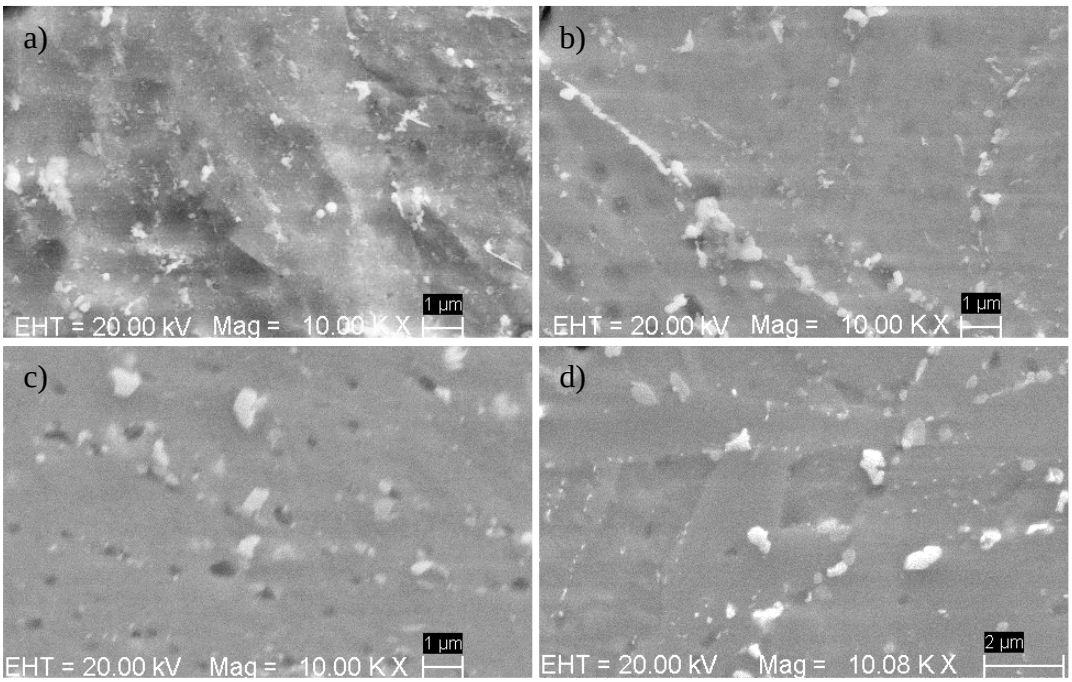

Figure 4.18 SEM micrograph showing the microstructure of ZL3 LY in a) the virgin state, b) 3 000 h of ageing, c) 10 000 h of ageing, and d) 30 307 h of ageing.

In test material ZL3, which contains W and no Mo, the Laves-phase particles are of the type Fe_2W. Traces of Cr and Si can also be found. A typical EDX spectrum of Laves-

phase particles (this particular particle is from ZL3 HY aged for 30 307 hours), can be seen in *Figure 4.19*, where peaks of W and Fe are obvious.

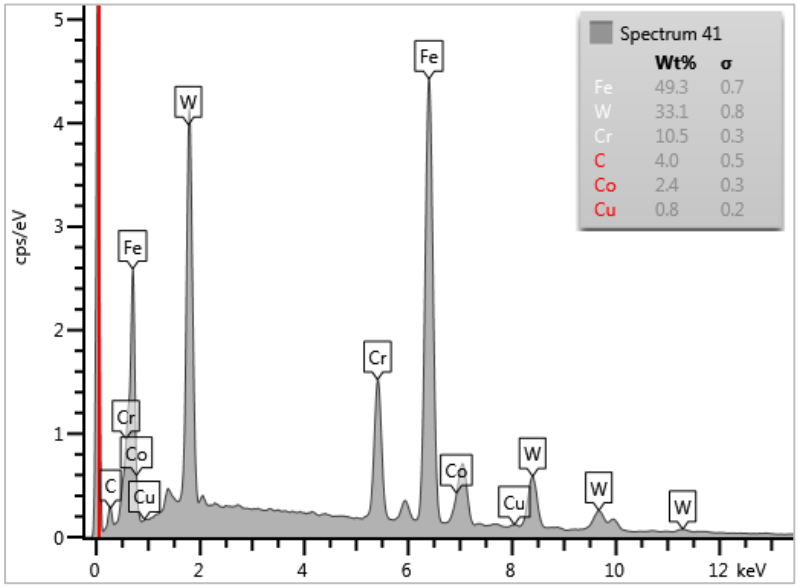

Figure 4.19 EDX spot analysis taken from ZL3 HY aged for 30 307 h, showing a typical spectrum of a Laves-phase particle.

In the TEM, Laves-phase are often the largest and darkest particles found. Three large Laves particles can be seen in *Figure 4.20*, which is from sample ZL3 LY aged for 30 307 hours. These types of large particles occur in all the samples studied. However, much smaller particles were also found.

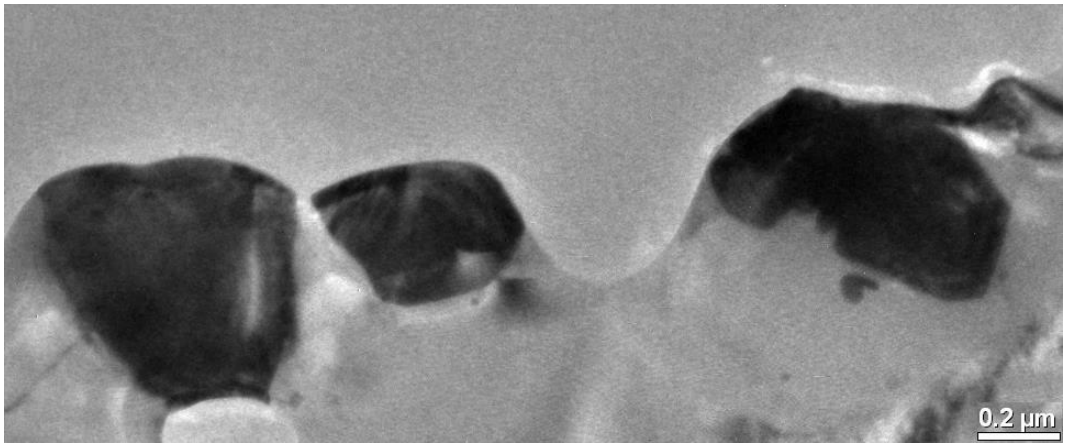

Figure 4.20 TEM micrograph showing three large Laves particles in sample ZL3 LY aged for 30 307 h.

The variation of the size of the Laves-phase can be seen in *Figure 4.21*, which shows the area distribution of Laves-phase depending on tempering temperature and ageing time. At the ageing time of 3 000 hours, which is seen in *Figure 4.21 a)* and *c)*, the x-axis ranges mostly between 0.002 µm^2 and 0.021 µm^2. The particles in HY are centred around the lower end of the x-axis, while the particles in LY largely appear at the last column of >0.021 µm^2.

After the samples have been aged for 30 307 hours, see *Figure 4.21 b)* and *d)*, the x-axis range mostly between 0.03 µm^2 and 0.13 µm^2. Thus, overall Laves particles found after 30 307 hours of ageing is larger than after 3 000 hours of ageing. Furthermore, for HY the particles are centred around the lower end of the x-axis, while for LY the particles are centred around the higher end of the x-axis.

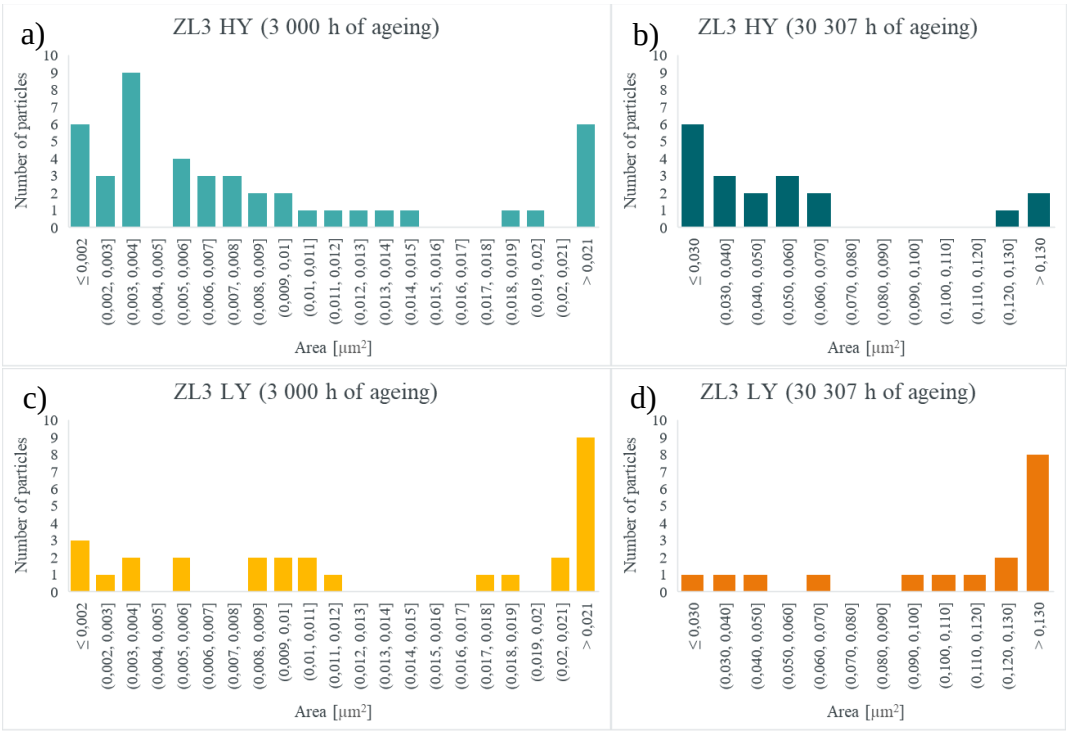

Figure 4.21 Area distribution of Laves-phase, a) ZL3 HY for 3 000 h of ageing, b) ZL3 HY for 30 307 h of ageing, c) ZL3 LY for 3 000 h of ageing, and d) ZL3 LY for 30 307 h of ageing.

The average particle area of Laves particles, with standards deviation, is shown in *Table 4.3*. In HY the average area of Laves-phase is 0.018 µm^2 after 3 000 hours of ageing and 0.071 µm^2 after 30 307 hours of ageing. Meanwhile in LY the average area is 0.029 µm^2 after 3 000 hours of ageing and increases to 0.162 µm^2 after 30 307 hours of ageing. Thus, Laves-phase is significantly affected by tempering temperature. At 3 000 hours of ageing, Laves particles in LY are almost 50% larger than the Laves particles in HY. After 30 307 hours of ageing, the growth of Laves-phase in LY compared to HY is even more prominent. The Laves particles in LY doubled the size than those in HY.

Table 4.3 The average particle area and the standards deviation for Laves-phase depending on tempering temperature (HY and LY) and ageing time (3 000 hours of ageing and 30 307 hours of ageing).

	ZL3 HY		ZL3 LY	
Ageing time [h]	Area [µm^2]	Standard deviation	Area [µm^2]	Standard deviation
3 000	0.018	0.036	0.029	0.048
30 307	0.071	0.094	0.162	0.103

4.5.3 Z-phase, Z/MX and MX particles

MX particles are one of the most effective precipitates for strengthening in 9–12% Cr steels. Z-phase, on the other hand, are conventionally considered detrimental particles, since big Z-phase particles are formed by consuming the beneficial MX particles. The idea of Z-phase strengthened steel is to use Z-phase as strengthening precipitates, through fast nucleation and fine distribution. Thus, MX particles and Z-phase are both seen as beneficial particles in this case. Therefore, these particles are evaluated together.

In test material ZL3, Z-phase is of the type CrTaN, while MX is either of the type Ta(C,N) or pure TaC. In *Figure 4.22*, Z-phase and MX particles can be seen, for the different tempering temperatures (HY and LY) and ageing times (3 000 hours and 30 307 hours). Particles referred to as Z/MX can also be seen. These are hybrid particles that have a composition somewhere in between MX and Z-phase. Specifically, they have the composition Ta(C,N), with a higher Cr content than regular MX particles.

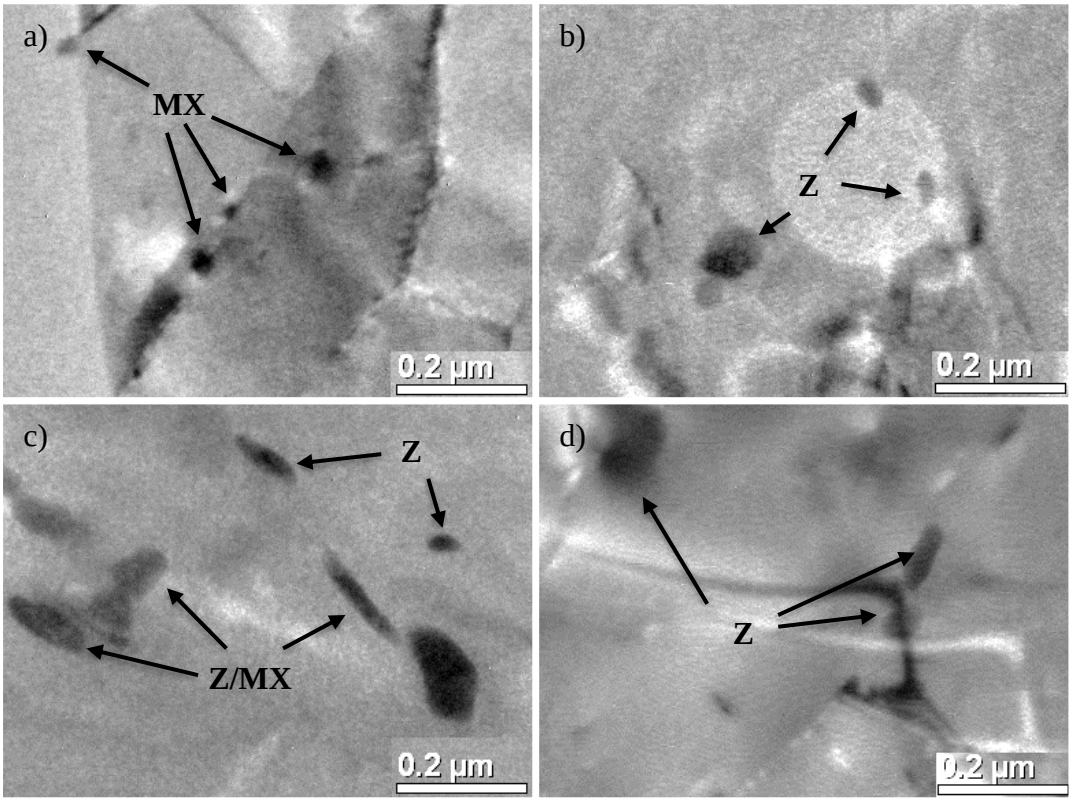

Figure 4.22 TEM micrographs a) ZL3 HY aged for 3 000 h, b) ZL3 HY aged for 30 307 h, c) ZL3 LY aged for 3 000 h and d) ZL3 LY aged for 30 307 h.

In *Figure 4.23*, the percentage of each type of particles, out of the total amount of Z-phase, Z/MX and MX particles studied are shown, for each tempering temperature and ageing time. Primary MX particles are not included in the result.

In the first column, ZL3 HY aged for 3 000 hours is shown, around 88% of the particles are MX particles. Only very few particles found are either Z-phase (3%) or Z/MX particles (8%). In the second column, which show ZL3 HY after 30 307 hours of ageing, there are only 4% MX particles left and around 94% are now Z-phase. The remaining 2% are Z/MX particles.

Meanwhile, in ZL3 LY aged for 3 000 hours, shown in the third column, MX particles make up 47% and Z/MX particles makes up 44% of the particles studied. Z-phase reaches 8% in this sample. In the fourth column, ZL3 LY aged for 30 307 hours is shown. 100% of the particles studied in this sample are Z-phase. Thus, it is shown that Z-phase transform from MX particles after a shorter ageing time in LY compared to HY.

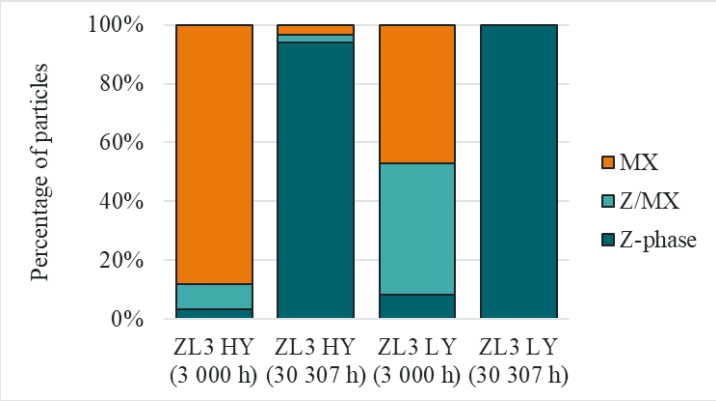

Figure 4.23 Diagram showing percentage of Z-phase, Z/MX and MX particles found in each sample.

The combined area distribution of Z-phase, Z/MX and MX particles can be seen in *Figure 4.24*. The x-axis for the shown diagrams, range between 0.001 µm^2 and 0.011 µm^2, with the first and last stands for ≤0.001 µm^2 and >0.011 µm^2, respectively. After 3 000 hours of ageing, both the particles in HY and LY are centred around the lower end of the x-axis. When the ageing time is increased to 30 307 hours, the particles in HY are still mostly centred around the lower end of the x-axis, while the particles in LY have gained a second peak at the higher end of the x-axis.

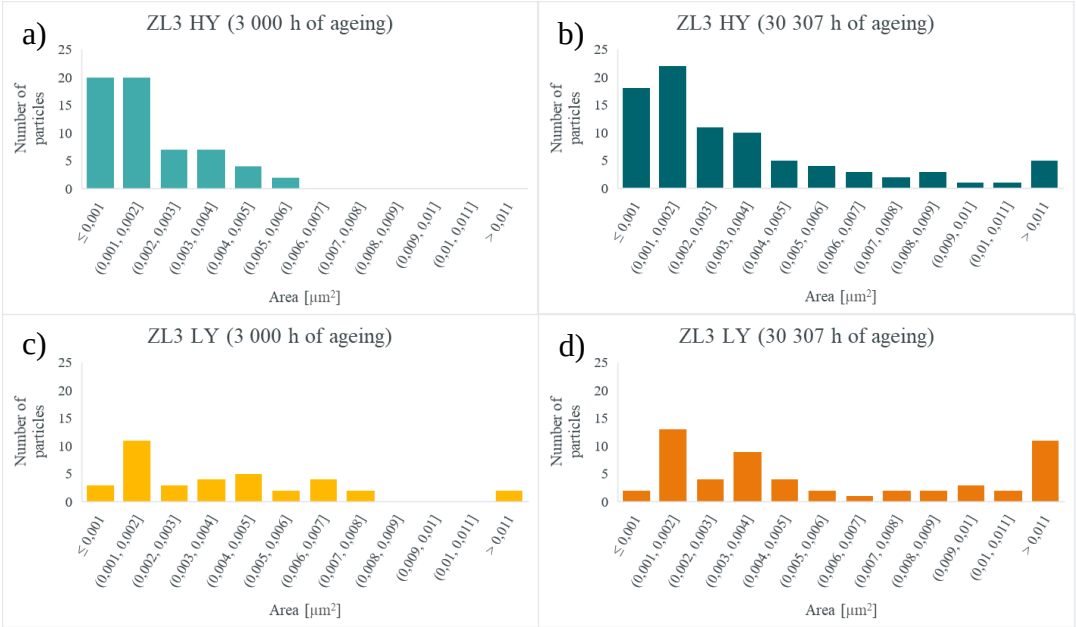

Figure 4.24 The area distribution of all Z-phase, Z/MX and MX particles together, a) ZL3 HY for 3 000 h of ageing, b) ZL3 HY for 30 307 h of ageing, c) ZL3 LY for 3 000 h of ageing and d) ZL3 LY for 30 307 h of ageing.

The combined average area for Z-phase, Z/MX and MX, with standards deviation, is shown in *Table 4.4*. In HY the average area is 0.0018 µm^2 after 3 000 hours of ageing and increases to 0.0038 µm^2 after 30 307 hours of ageing. Meanwhile in LY the average area is 0.0040 µm^2 after 3 000 hours of ageing and 0.0064 µm^2 after 30 307 hours of ageing. Thus, the combined average particle area for Z-phase, Z/MX and MX particles is lower in HY compared with LY.

Table 4.4 The combined average particle area and the standards deviation for Z-phase, Z/MX and MX particles depending on tempering temperature (HY and LY) and ageing time (3 000 hours of ageing and 30 307 hours of ageing).

	ZL3 HY		ZL3 LY	
Ageing time [h]	Area [µm^2]	Standard deviation	Area [µm^2]	Standard deviation
3 000	0.0018	0.0014	0.0040	0.0047
30 307	0.0038	0.0036	0.0064	0.0057

4.6 Previous results from atom probe tomography

Previous APT results obtained by Rashidi et al. [42], showed MX particles in samples ZL3 HY (*Figure 4.25*) and LY (*Figure 4.26*), in the virgin state. In both samples, MX particles of the type Ta(C,N) can be seen. ZL3 have a high C content, which is also reflected by the C and N content in MX particles, since C is dominant over N. However, pure TaN particles were also found. The Cr content is rather evenly distributed in the matrix, suggesting that Z-phase is not found in the particles shown.

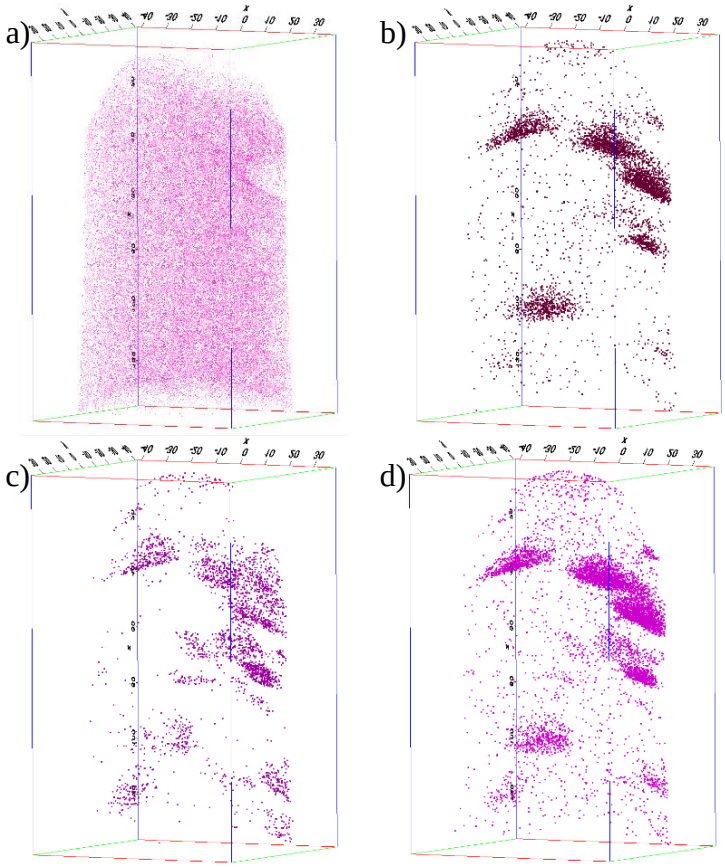

Figure 4.25 APT result showing sample ZL3 HY in the virgin state, a) Cr ion map, b) C ion map, c) TaN ion map, and d) Ta ion map.

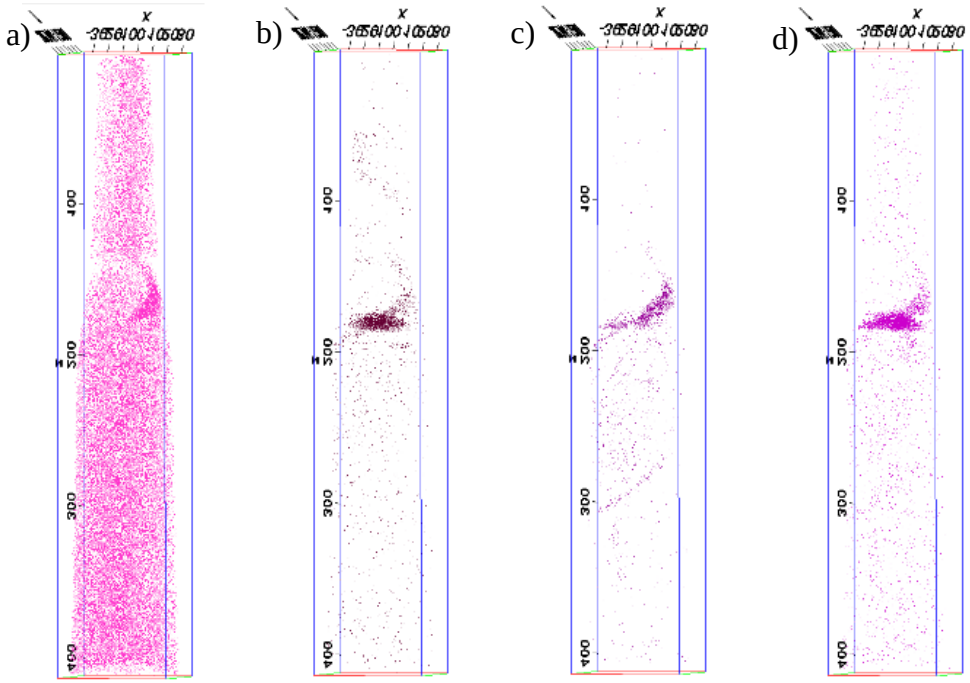

Figure 4.26 APT result showing sample ZL3 LY in the virgin state, a) Cr ion map, b) C ion map, c) TaN ion map, and d) Ta ion map.

5 Discussion

In the following chapter the results are discussed in relation to previous findings from the literature study. This chapter finishes with an overall discussion of the correlation between microstructure evolution and creep resistance in test material ZL3.

5.1 The effect of tempering temperature on creep and mechanical properties

Creep curves for ZL3 at 650°C show that HY perform better than LY. This is in line with a report of the effect of varying tempering temperatures on the stress rupture properties of a 9% Cr steel, done by Maddi et al. [43]. At a higher tempering temperature, the martensitic structure recovers to a larger extent than at a lower temperature, which reduces the density of mobile dislocations. A reduced dislocation density negatively affects the creep strength. However, for ZL3, it is found that the slope of the creep curves for HY are much steeper compared to those of LY. The higher density of the mobile dislocations in samples with lower tempering temperatures, results in a more rapid evolution of the microstructure, which in turn results in the steeper creep curves [43].

In steel ZL3, comparison of tempering temperature, HY and LY, show that the initial values for hardness, yield strength and ultimate tensile strength is higher in ZL3 HY. Though ductility is lower in HY. This agrees with the results shown by Barbadikar et al. [44], in a study of the microstructure and mechanical properties of a 9% Cr steel, at different tempering temperatures. In the case of ZL3, thermal ageing was also used, to test the above-mentioned mechanical properties, at different ageing times, which showed that all values converge with ageing time. This means that comparison between crept and thermally aged samples are possible.

Additionally, the average prior austenite grain size was studied. The grain size has a close relationship with mechanical properties, since smaller grains result in an increase of strength, ductility and toughness [13]. In ZL3 HY the PAG size were 59±4 µm and in ZL3 HY they were 61±3 µm. Since the grain size only differs slightly, within the error bars of the results, it is concluded that the tempering temperature does not have a significant impact on the prior austenite grain size.

5.2 The distribution of boron nitride particles

BN particles form during the slow cooling after solidification [23,24]. They are stable particles that should not be affected by either tempering temperature or ageing time. However, in the samples of steel ZL3 an unexpected trend was discovered. The BN particles seem to be bigger and have a higher area fraction in the virgin state compared to the aged samples. To confirm this, extra samples at the virgin state, for both tempering temperatures, HY and LY, were studied. BN particles were still found to have a higher area fraction in the new samples, though they were much more in line with the aged samples.

A correlation between the area fraction of BN particles and ageing time is still unlikely. The difference that was observed between different samples, were also observed at different sites in the same sample. It is more likely that there is an overall uneven

distribution of BN particles in the original bar, from which the samples for different ageing experiments were taken. However, the uneven distribution of BN particles potentially leads to local variations in secondary particles. Since consumption of B affects the coarsening behaviour of particles such as $M_{23}C_6$ and Z-phase precipitates [24]. This could possibly lead to that secondary particles grow coarser and have a decreased precipitation hardening effect in the areas with higher area fraction of BN particles.

5.3 Nucleation and growth of $M_{23}C_6$ particles

$M_{23}C_6$ particles are known to be beneficial carbides in 12% Cr steel. They precipitate at the prior austenite grain boundaries and the martensite lath or subgrain boundaries [17,18,19]. They pin the boundaries and contribute to precipitation hardening, and increased creep strength [1]. In ZL3, $M_{23}C_6$ particles was found to occur as both single particles and clusters of particles. Laves-phase were often found in the vicinity of them, which is also reported by Prat et al. [17].

During investigation of $M_{23}C_6$ particles it was found that in both of the cases, HY and LY, the particles grow very slowly, which is in agreement with simulations of coarsening of $M_{23}C_6$ particles by DICTRA done by Prat et al. Furthermore, simulations by TC-PRISMA by Prat et al. [17], show that the precipitation of $M_{23}C_6$ particles begins at the moment the tempering treatment take off and after a rather short time the precipitation were complete.

Particles in LY are on average bigger than those in HY, which is explained by the higher tempering temperature for LY. A higher tempering temperature results in faster nucleation and growth. However, in both cases the particles grow very slowly, and while the tempering temperature affect how large the particles grow initially, it barley affect how much they continue to grow, i.e. coarsen, later on during ageing. This means that for both HY and LY, $M_{23}C_6$ particles remains to be beneficial carbides in ZL3.

5.4 Nucleation and growth of Laves-phase

In steel ZL3 very few Laves-phase were found in the virgin state of the steels, which is expected since Laves-phase are secondary particles that form during service [22]. For both HY and LY, small Laves-phase particles had formed after 3 000 hours of ageing. At this stage the particles look more needle-like. The appearance of Laves particles in the SEM after 10 000 and 30 307 hours of ageing have much in common with each other. At this stage they are larger, irregular in shape and are formed close to $M_{23}C_6$ carbides, which is in line with other studies [17,21].

It is reported by Di Gianfrancesco et al. [22], that Laves-phase form relatively quickly between 1 000–10 000 hours of service at 600°C–650°C. This would explain the large change of Laves-phase between samples aged 3 000 and 10 000 hours, while the difference between 10 000 and 30 307 hours seem to be less. A more in depth analysis of Laves-phase in the TEM were done for samples aged for 3 000 and 30 307 hours. It was found that Laves-phase are, at 3 000 hours of ageing, almost 50% larger in LY compared to HY. This was even more prominent after 30 307 hours of ageing.

Formation of Laves-phase causes depletion of W from the matrix, which decrease the solid solution strengthening effect [1,21]. On the other hand, Laves-phase tend to form clusters along the martensite lath boundaries or sub-grain boundaries [17,21], which provides precipitation hardening and creep resistant at the beginning of their formation [21]. Consequently, the benefit and drawback of Laves-phase have been debated [21]. In Z-phase strengthened steels, the aim is to keep the Laves particles as small as possible. Therefore, it can be concluded, due to the prominent growth of Laves-phase in LY compared to HY, that Laves-phase is significantly affected by the tempering temperature. The positive effect of Laves-phase appears to last far longer in HY than in LY.

5.5 MX to Z-phase transformation

It was suggested that Z-phase can transform from both M_2X and MX particles [31]. In the case of formation of M_2X particles, they are influenced by the tempering temperature [25,26]. In 9% Cr steels it was found that a lower tempering temperature promotes the formation of M_2X instead of MX [26]. However, the stability of M_2X particles is also influenced by the Cr content, and thus as a result M_2X particles have been found in 12% Cr steels even at higher tempering temperatures [26]. In the case of ZL3, only two M_2X particles were found in the present study. They were found in sample ZL3 LY aged for 30 307 hours. Since LY is the version of ZL3 steel with the higher tempering temperature, it suggests that there are M_2X particles most likely in the HY version too. However, the small number of M_2X particles found in ZL3 indicates that Z-phase are unlikely to transform from M_2X particles in this particular steel.

Transformation of Z-phase particles from MX occur either through direct transformation from Cr-enriched MX particles to Z-phase or by nucleation and growth from the MX particles [28]. For Ta-based Z-phase it has been suggested that Z-phase transformation from Ta(C,N) particles through in-diffusion of Cr and out-diffusion of C, while Z-phase transformation from TaN only needs in-diffusion of Cr [23].

Earlier APT results by Rashidi et al. [42], of ZL3 in the virgin state, show that MX particles have a composition of either Ta(C,N) or pure TaN. EDX results from TEM, for samples aged for 3 000 and 30 307 hours, show no MX particles of the type TaN. Since TaN particles only needs in-diffusion of Cr, the transformation of Z-phase is quicker [23]. Therefore, it is likely that the Z-phase particles found in samples ZL3 HY and LY at 3 000 hours ageing, were transformed from MX particles of the type TaN.

The majority of the particles found in ZL3 HY at 3 000 hours of ageing, are still MX particles. Particles in ZL3 LY at the same ageing time, are mostly either MX or Z/MX particles. Z/MX particles are a hybrid particle, that have a composition between that of Z-phase and MX. After 30 307 hours of ageing, for HY and LY, more or less all MX particles have transformed in to Z-phase. Thus, it is shown that Z-phase start to transform from MX particles after a shorter ageing time in LY compared to HY.

By evaluating Z-phase, Z/MX and MX particles together, with the exception of primary MX particles, it was shown that the distribution of the particle area was located at the lower side for HY than LY. Consequently, this leads to a combined average particle area that is lower in HY compared with LY.

5.6 The correlation between microstructure evolution and creep resistance

Tempering is an important step to reduce the residual stresses left in the material after quenching, and the tempering temperature chosen has a substantial effect on the microstructure and the resulting mechanical properties. A higher tempering temperature has shown to decrease hardness and strength, and increase ductility [1,11]. This was also found to be the case for steel ZL3. However, with thermal ageing, the values of their mechanical properties, converge with ageing time.

In creep testing the martensitic structure recovered to a larger extent in the samples with a higher tempering temperature than a lower tempering temperature, which reduced the mobile dislocation density [43]. The reduction in dislocation density for ZL3 LY made it perform worse in the beginning of creep. However, the higher density of mobile dislocations in HY makes the creep curves steeper in the later stages of creep (after ~10 hours). Still, HY performs better in terms of creep testing.

Tempering temperature and ageing time were found to have insignificant effect on BN particles, slight effect on $M_{23}C_6$ particles, and significant effect on both Laves-phase, and MX to Z-phase transformation. Overall, secondary particles in HY grow slower and have an average particle area smaller than those in LY.

Despite ZL3 HY's superior microstructure regarding nano-sized particles, values for mechanical properties, again, converge with ageing time. It seems that the higher density of mobile dislocations combined with smaller particles, in HY, makes HY perform significantly better in the beginning. However, with time the small particles cannot maintain the high dislocation density in the later stages of creep and thermal ageing, in HY. This means that HY only outperforms LY for a certain time.

6 Conclusion

The aim of this project was to get a deeper understanding between the correlation between microstructure evolution and creep resistance in a new generation of Z-phase strengthened 12% Cr steels. To achieve this the effect of heat treatment on nano-sized particles and how they evolve at high temperatures were studied. This could potentially lead to a solution to the conflict between creep and corrosion resistance at 650°C for these steels. The conclusions based on this goal are the following:

- HY performs better in terms of creep strength. Hardness, tensile strength and impact toughness for HY and LY converge after 30 307 h.
- Interesting trend was found on the area fraction of BN particles: they appear to decrease with ageing time. However, BN particles are very stable and a correlation with ageing time is very unlikely.
- $M_{23}C_6$ particles grow very slowly and the growth rate is barley affected by the tempering temperature of HY and LY.
- Laves-phase is significantly affected by tempering temperature. At 30 307 hours of ageing, Laves particles in LY have doubled the size of those in HY.
- Z-phase are formed from MX particles after a shorter ageing time in LY compared to HY. Z-phase and MX particles also have a lower average particle area for HY than LY.
- ZL3 HY has superior microstructure regarding nano-sized particles, thus HY outperforms LY.

6.1 Future outlook

The extractive carbon replica technique described in Appendix 1, is a method that, if working properly, gives good statistics of particle analyses without inference from the magnetic steel matrix in the TEM. Further efforts should be made to succeed with this method in the future.

Due to time constraint, samples aged for 10 000 hours were not studied in TEM. These samples should be added for better understanding of the evolution of nano-sized particles.

Around 110 particles for each sample were studied in TEM. For overall better statistics, more particles should be studied.

7 References

[1] M. Rashidi, "Microstructure of Z-phase strengthened steels," Chalmers University of Technology, 2017.

[2] H. K. Danielsen and J. Hald, "Influence of Z-phase on Long-term Creep Stability of Martensitic 9 to 12% Cr Steels," *VGB powertech*, vol. 89, pp. 68–73, 2009.

[3] H. Bhadeshia and R. Honeycomb, "Iron and its Interstitial Solutions," in *Steels - Microstructure and Properties*, 4th Editio., Oxford, UK: Elsevier Ltd, 2017, pp. 1–22.

[4] A. . Elshennawy and G. . Weheba, "Material Properties and Testing," in *Manufacturing Processes and Materials*, 5th Editio., US: Society of Manufacturing Engineers, 2015, pp. 23–55.

[5] M. E. Kassner and M.-T. Pérez-Prado, *Fundamentals of Creep in Metals and Alloys*, 1st Editio. Oxford, UK: Elsevier, 2004.

[6] F. Abe, "Introduction," in *Creep-resistant steels*, 1st Editio., F. Abe, T.-U. Kern, and R. Viswanathan, Eds. Cambridge, England: Woodhead Publishing Limited, 2008, pp. 3–14.

[7] H. Oikawa and Y. Iijima, "Diffusion behaviour of creep-resistant steels," in *Creep-resistant steels*, 1st editio., F. Abe, T.-U. Kern, and R. Viswanathan, Eds. Cambridge, England: Woodhead Publishing Limited, 2008, pp. 241–264.

[8] W. Hoffelner, "Development and Application of Nano-Structured Materials in Nuclear Power Plants," in *Understanding and Mitigating Ageing in Nuclear Power Plants*, 1st Editio., P. G. Tipping, Ed. Cambridge, England: Woodhead Publishing Limited, 2010, pp. 581–605.

[9] R. G. Faulkner, "Grain boundaries in creep-resistant steels," in *Creep-resistant steels*, 1st Edit., F. Abe, T.-U. Kern, and R. Viswanathan, Eds. Cambridge, England: Woodhead Publishing Limited, 2008, pp. 329–349.

[10] E. Kozeschnik and I. Holzer, "Precipitation during heat treatment and service: characterization, simulation and strength contribution," in *Creep-resistant steels*, 1st Edit., F. Abe, T.-U. Kern, and R. Viswanathan, Eds. Cambridge, England: Woodhead Publishing Limited, 2008, pp. 305–328.

[11] F. C. Campbell, Ed., "Heat treatment," in *Metals Fabrication - Understanding the Basics*, 1st Editio., Ohio, US: ASM International, 2013, pp. 271–324.

[12] H. Bhadeshia and R. Honeycomb, "Formation of Martensite," in *Steels - Microstructure and Properties*, 4th Editio., Oxford, UK: Elsevier Ltd, 2017, pp. 135–178.

[13] A. C. Reardon, "Mechanical Properties and Strengthening Mechanisms," in *Metallurgy for the Non-Metallurgist*, 2nd Editio., Ohio, US: ASM International, 2011, pp. 49–71.

[14] F. Abe, "Strengthening mechanisms in steel for creep and creep rupture," in *Creep-resistant steels*, 1st edit., F. Abe, T.-U. Kern, and R. Viswanathan, Eds. Cambridge, England: Woodhead Publishing Limited, 2008, pp. 279–304.

[15] H. K. Danielsen, "Z-phase in 9-12% Cr Steels," Technical University of Denmark, 2007.

[16] D. A. Porter, K. E. Easterling, and M. Y. Sherif, "Diffusional Transformations in Solids," in *Phase Transformations in Metals and Alloys*, 3rd ed., Boca Raton, US: CRC Press, 2009, pp. 261–382.

[17] O. Prat, J. García, D. Rojas, J. P. Sanhueza, and C. Camurri, "Study of nucleation, growth and coarsening of precipitates in a novel 9%Cr heat resistant steel: Experimental and modeling," *Mater. Chem. Phys.*, vol. 143, no. 2, pp. 754–

764, 2014.
[18] O. Prat, J. Garcia, D. Rojas, C. Carrasco, and A. R. Kaysser-Pyzalla, “Investigations on coarsening of MX and M23C6 precipitates in 12% Cr creep resistant steels assisted by computational thermodynamics,” *Mater. Sci. Eng. A*, vol. 527, no. 21–22, pp. 5976–5983, 2010.
[19] N. qiong Zhu, L. Lu, Y. lin He, L. Li, and X. gang Lu, “Coarsening of M23C6 Precipitates in an Fe-Cr-C Ternary Alloy,” *J. Iron Steel Res. Int.*, vol. 19, no. 9, pp. 62–67, 2012.
[20] M. Hättestrand and H.-O. Andrén, “Boron distribution in 9-12% chromium steels,” *Mater. Sci. Eng. A*, vol. 270, no. 1, pp. 33–37, 1999.
[21] O. Prat, J. Garcia, D. Rojas, G. Sauthoff, and G. Inden, “The role of Laves phase on microstructure evolution and creep strength of novel 9%Cr heat resistant steels,” *Intermetallics*, vol. 32, pp. 362–372, 2013.
[22] A. Di Gianfrancesco, S. Tiberi Vipraio, and D. Vendit, “Long term microstructural evolution of 9-12%Cr steel grades for steam power generation plants,” *Procedia Eng.*, vol. 55, pp. 27–35, 2013.
[23] M. Rashidi, L. Johansson, H. O. Andrén, and F. Liu, “Microstructure and mechanical properties of two Z-phase strengthened 12%Cr martensitic steels: the effects of Cu and C,” *Mater. Sci. Eng. A*, vol. 694, no. March, pp. 57–65, 2017.
[24] M. Rashidi, R. Lawitzki, H.-O. Andrén, and F. Liu, “Tantalum and niobium based Z-phase in a Z-phase strengthened 12% Cr steel,” in *EPRI 8th International Conference on Advances in Materials Technology for Fossil Power Plants*, 2016.
[25] R. Ishii, Y. Tsuda, M. Yamada, and K. Kimura, “Fine precipitates in high chromium heat resisting steels,” *J. Iron Steel Inst. Japan*, vol. 88, no. 1, pp. 36–43, 2002.
[26] K. Suzuki, M. Tabuchi, K. Kimura, K. Sawada, and H. Kushima, “Effect of tempering temperature on Z-phase formation and creep strength in 9Cr–1Mo–V–Nb–N steel,” *Mater. Sci. Eng. A*, vol. 480, no. 1–2, pp. 558–563, 2007.
[27] K. Sawada, H. Kushima, and K. Kimura, “Z-phase Formation during Creep and Aging in 9–12% Cr Heat Resistant Steels,” *ISIJ Int.*, vol. 46, no. 5, pp. 769–775, 2006.
[28] L. Cipolla, H. K. Danielsen, D. Venditti, P. E. Di Nunzio, J. Hald, and M. A. J. Somers, “Conversion of MX nitrides to Z-phase in a martensitic 12% Cr steel,” *Acta Mater.*, vol. 58, no. 2, pp. 669–679, 2010.
[29] H. K. Danielsen and J. Hald, “Tantalum-containing Z-phase in 12%Cr martensitic steels,” *Scr. Mater.*, vol. 60, no. 9, pp. 811–813, 2009.
[30] R. Agamennone, W. Blum, C. Gupta, and J. K. Chakravartty, “Evolution of microstructure and deformation resistance in creep of tempered martensitic 9-12%Cr-2%W-5%Co steels,” *Acta Mater.*, vol. 54, no. 11, pp. 3003–3014, 2006.
[31] M. Y. Kim *et al.*, “Mechanism for Z-phase formation in 11CrMoVNbN martensitic heat-resistant steel,” *Mater. Charact.*, vol. 129, no. April, pp. 40–45, 2017.
[32] T. H. G. Megson, “Properties of Engineering Materials,” in *Structural and Stress Analysis*, 2nd editio., Oxford, UK: Elsevier, 2005, pp. 188–208.
[33] “Vickers hardness test (ISO 6507-1:2018),” *Int. Organ. Stand.*, 2018.
[34] “Tensile testing (ISO 6892-1:2017),” *BSI Stand. Publ.*, 2017.
[35] “Charpy pendulum impact test (ISO 148-1:2017),” *Int. Organ. Stand.*, 2017.
[36] G. F. Vander Voort, “Light Microscopy,” in *Metallography: Principles and Practice*, New York, US: McGraw-Hill Book Company, 1984, pp. 267–333.

[37] J. I. Goldstein, D. E. Newbury, P. Echlin, D. C. Joy, and E. Lifshin, "Introduction," in *Scanning Electron Microscopy and X-Ray Microanalysis*, New York, US: Plenum Publishing, 1981, pp. 1–18.
[38] C. B. Carter and D. B. Williams, "The transmission electron microscope," in *Transmission Electron Microscopy: A Textbook for Materials Science*, 2nd Editio., New York, US: Springer, 2009, pp. 3–22.
[39] R. Brydson, A. Brown, L. G. Benning, and K. Livi, "Analytical Transmission Electron Microscop," in *Spectroscopic Methods in Mineralogy and Materials Sciences*, G. S. Henderson, D. R. Neuville, and R. T. Downs, Eds. Chantilly, Virginia, US: De Gruyter, 2015, pp. 219–270.
[40] H. Colpaert, "Metallographic Technique—Electron Microscopy and Other Advanced Techniques," in *Metallography of Steels - Interpretation of Structure and the Effects of Processing*, 4th Editio., US: ASM International, 2018, pp. 85–99.
[41] "Standard Test Methods for Determining Average Grain Size (ASTM E112-13)," *ASTM Int.*, pp. 1–11, 2013.
[42] M. Rashidi, L. Johansson, H. O. Andrén, and F. Liu, "Unpublished result."
[43] L. Maddi, A. R. Ballal, D. R. Peshwe, R. K. Paretkar, K. Laha, and M. D. Mathew, "Effect of tempering temperature on the stress rupture properties of Grade 92 steel," *Mater. Sci. Eng. A*, vol. 639, pp. 431–438, 2015.
[44] M. D. Mathew *et al.*, "Effect of normalizing and tempering temperatures on microstructure and mechanical properties of P92 steel," *Int. J. Press. Vessel. Pip.*, vol. 132–133, pp. 97–105, 2015.
[45] J. Ayache, L. Beaunier, J. Boumendil, G. Ehret, and D. Laub, "Replica Techniques," in *Sample Preparation Handbook for Transmission Electron Microscopy*, 2010, pp. 229–256.

Appendix 1: Extractive carbon replica

Extractive carbon replica technique is a specimen preparation method for TEM. The idea is to remove particles from the sample surface and adhere them onto a carbon film. It is mostly used for metallic materials. The advantages of this technique are that good statistical analyses of particles can be achieved; particular for ferromagnetic materials; magnetic inference in the TEM by the matrix can be avoided. A drawback is that the particles loss the direct relationship that they have with the matrix [45].

The procedure starts with mounted and freshly polished samples, which then undergo over-etching to make the particles stand out from the substrate. The surface was then coated with a carbon film using the carbon sputtering coating machine Edwards S150B. The film is cut into 2 x 2 mm big squares. The substrate is then electropolished to release the carbon film. Water's surface tension is used to lift the small replica squares [45]. The finished carbon replica samples float on the water surface and get "fished out" by a copper grid used for TEM.

Table A1.1 shows the parameters used for depositing the carbon film. In *Figure A1.1*, carbon films with different layer thickness are shown. The ideal layer thickness is between b) and c). Electropolishing etchant used were 95% ethanol and 5% HCl. Only one sample, ZL3 HY aged for 3 000 hours, were successfully prepared during this project. An image taken in the TEM, of this sample, can be seen in *Figure A1.2*.

Table A1.1 Parameters used for carbon coating for the extractive carbon replica technique.

Carbon ends:	1 mm flat ends
Vacuum:	10^{-1} Torr
Distance:	25-30 mm
Time:	90-120 s

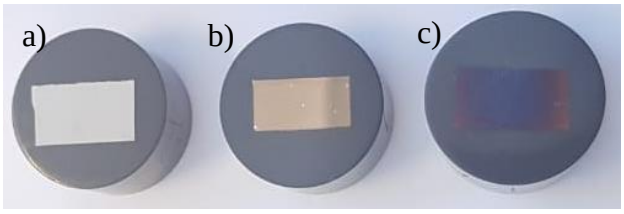

Figure A1.1 Samples coated with a carbon film, a) very thin layer, b) thin–medium thin layer, and c) thick layer.

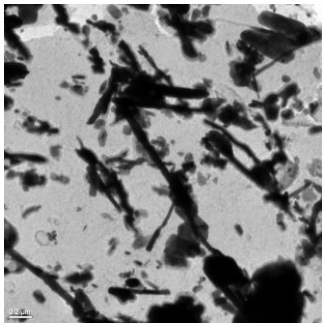

Figure A1.2 TEM micrograph of sample ZL3 HY aged for 3 000 hours, showing particles extracted with carbon replica technique.